



Herschel and *Hubble* Study of a Lensed Massive Dusty Starbursting Galaxy at $z \sim 3$ *

H. Nayyeri¹, A. Cooray¹, E. Jullo², D. A. Riechers³, T. K. D. Leung³, D. T. Frayer⁴, M. A. Gurwell⁵, A. I. Harris⁶, R. J. Ivison^{7,8}, M. Negrello⁹, I. Oteo^{7,8}, S. Amber¹⁰, A. J. Baker¹¹, J. Calanog¹², C. M. Casey¹³, H. Dannerbauer^{14,15}, G. De Zotti¹⁶, S. Eales¹⁷, H. Fu¹⁸, M. J. Michałowski⁸, N. Timmons¹, and J. L. Wardlow¹⁹

¹ Department of Physics and Astronomy, University of California Irvine, Irvine, CA, USA

² Laboratoire d'Astrophysique de Marseille, Pôle de l'Étoile Site de Château-Gombert 38, rue Frédéric Joliot-Curie F-13388 Marseille cedex 13, France

³ Department of Astronomy, Cornell University, Ithaca, NY, 14853, USA

⁴ National Radio Astronomy Observatory, Green Bank, WV, 24944, USA

⁵ Harvard-Smithsonian Center for Astrophysics, 60 Garden St., MS 42, Cambridge, MA 02138 USA

⁶ Department of Astronomy University of Maryland College Park, MD 20742, USA

⁷ European Southern Observatory, Karl-Schwarzschild-Strasse 2, D-85748 Garching, Germany

⁸ Institute for Astronomy, University of Edinburgh, Blackford Hill, Edinburgh EH9 3HJ, UK

⁹ School of Physics and Astronomy, Cardiff University, The Parade, Cardiff CF24 3AA, UK

¹⁰ Department of Physical Sciences, The Open University, Milton Keynes, MK7 6AA, UK

¹¹ Department of Physics & Astronomy, Rutgers, the State University of New Jersey, 136 Frelinghuysen Road, Piscataway, NJ 08854-8019, USA

¹² Department of Physical Sciences, San Diego Miramar College, San Diego CA, 92126, USA

¹³ Department of Astronomy, University of Texas at Austin, RLM 16.218 2515 Speedway, Stop C1400, Austin, TX 78712-1205, USA

¹⁴ Instituto de Astrofísica de Canarias (IAC), E-38205 La Laguna, Tenerife, Spain

¹⁵ Universidad de La Laguna, Dpto. Astrofísica, E-38206 La Laguna, Tenerife, Spain

¹⁶ INAF-Osservatorio Astronomico di Padova, I-35122 Padova, Italy

¹⁷ School of Physics & Astronomy, Cardiff University, Cardiff, UK

¹⁸ Department of Physics & Astronomy, University of Iowa, Iowa City, Iowa 52242, USA

¹⁹ Centre for Extragalactic Astronomy, Department of Physics, Durham University, South Road, Durham, DH1 3LE, UK

Received 2017 January 4; revised 2017 May 20; accepted 2017 June 18; published 2017 July 25

Abstract

We present the results of combined deep Keck/NIRC2, *HST*/WFC3 near-infrared, and *Herschel* far-infrared observations of an extremely star-forming dusty lensed galaxy identified from the *Herschel* Astrophysical Terahertz Large Area Survey (*H*-ATLAS J133542.9+300401). The galaxy is gravitationally lensed by a massive *WISE*-identified galaxy cluster at $z \sim 1$. The lensed galaxy is spectroscopically confirmed at $z = 2.685$ from detection of CO (1 \rightarrow 0) by GBT and from detection of CO (3 \rightarrow 2) obtained with CARMA. We use the combined spectroscopic and imaging observations to construct a detailed model of the background dusty lensed submillimeter galaxy (SMG), which allows us to study the source plane properties of the target. The best-fit lens model provides magnifications of $\mu_{\text{star}} = 2.10 \pm 0.11$ and $\mu_{\text{dust}} = 2.02 \pm 0.06$ for the stellar and dust components, respectively. Multiband data yield a magnification-corrected star formation rate of $1900(\pm 200) M_{\odot} \text{yr}^{-1}$ and a stellar mass of $6.8_{-2.7}^{+0.9} \times 10^{11} M_{\odot}$, consistent with a main sequence of star formation at $z \sim 2.6$. The CO observations yield a molecular gas mass of $8.3(\pm 1.0) \times 10^{10} M_{\odot}$, similar to the most massive star-forming galaxies, which together with the high star formation efficiency, are responsible for the intense observed star formation rates. The lensed SMG has a very short gas depletion timescale of ~ 40 Myr. The high stellar mass and small gas fractions observed indicate that the lensed SMG likely has already formed most of its stellar mass and could be a progenitor of the most massive elliptical galaxies found in the local universe.

Key words: gravitational lensing: strong – submillimeter: galaxies

1. Introduction

Understanding the formation of galaxies and their subsequent evolution with cosmic time is a fundamental goal of observational astronomy. Galaxies are believed to form in gas-rich environments (Dekel et al. 2009) and assemble their mass through constant gas accretion in secular evolutions (Dekel et al. 2009; Kruijssen et al. 2014; Narayanan et al. 2015), mergers (Kauffmann et al. 1993; Hopkins et al. 2008, 2013; Tacconi et al. 2008; Engel et al. 2010), or both (Kormendy & Kennicutt 2004; Genzel et al. 2008; Barro et al. 2013). The evolutionary track of galaxies is accompanied by various phases of star formation, which could be triggered by events such as mergers and sustained by processes such as gas accretion onto the potential wells of the underlying dark-matter

halos (Cole et al. 1994; Granato et al. 2004; Bower et al. 2006; Furlong et al. 2015). Studying the physical processes responsible for regulating star formation is crucial in getting a better understanding of galaxy formation and evolution (Law et al. 2009; Hemmati et al. 2014, 2015).

One of the main sites of star formation in the universe at high redshifts is submillimeter galaxies (SMGs; for a recent review, see Casey et al. 2014). These systems are rich in gas and dust and have measured star formation rates in excess of hundreds to a few thousand solar masses per year (Greve et al. 2005; Capak et al. 2008; Magnelli et al. 2012; Michałowski et al. 2017). These dusty galaxies are readily identified and studied in extragalactic surveys at long wavelengths (Blain et al. 1999; Elbaz et al. 2011; Leroy et al. 2013; Scoville et al. 2016; Hemmati et al. 2017) in which they are most luminous as the UV light emitted by the hot young stars (produced by intense star formation activity) is absorbed and re-radiated by dust.

* *Herschel* is an ESA space observatory with science instruments provided by European-led Principal Investigator consortia and with important participation from NASA.

Recent studies indicate a very rapid mass assembly and short duty cycles (starburst phase) for the high-redshift SMGs (Greve et al. 2005; Tacconi et al. 2006, 2008; Riechers et al. 2011b; Magnelli et al. 2012; Toft et al. 2014) with timescales as short as ~ 100 Myr. The high star formation rate is responsible for the mass build-up in SMGs. In fact, cosmological hydrodynamic simulations show that the SMGs are on average very massive and reside in $\sim 10^{13} M_{\odot}$ halos at $z \sim 2$ (Davé et al. 2010). This agrees with multiband observations of submillimeter samples of galaxies at similar redshifts with stellar masses as high as a few times $10^{11} M_{\odot}$ and a median of $7 \times 10^{10} M_{\odot}$ (Hainline et al. 2011). The rapid mass assembly in SMGs over short timescales followed by gas reservoir depletion due to intense star formation could possibly explain the origin of the most massive quiescent galaxies. In fact, recent studies have shown that the very high-redshift SMGs could indeed be the progenitors of the most massive quiescent systems (Nayyeri et al. 2014; Toft et al. 2014). A better understanding of the mass assembly and the underlying star formation responsible for it is achieved with the knowledge of the full spectral energy distribution (SED) of the galaxy. Given the amounts of dust, these systems are intrinsically faint at shorter wavelengths and become bright at longer wavelengths. Even with intrinsic luminosities of $\sim 10^{13} L_{\odot}$, identifications of SMGs at high redshifts are still challenging. Gravitational lensing provides a unique tool to study this obscured population of galaxies at high redshift. The signal boost provided by gravitational lensing and the increase in spatial resolution combined with robust lens modeling allow us to study the star-forming regions within these galaxies at sub-kiloparsec scales (Swinbank et al. 2010; Dye et al. 2015; Rybak et al. 2015; Swinbank et al. 2015). In fact, this tool has been successfully utilized in several recent works to study the physical properties of gas-rich star-forming systems at high redshift (Frayer et al. 1998, 1999; Ivison et al. 1998, 2000; Gavazzi et al. 2011; Riechers et al. 2011a; Swinbank et al. 2011; Bussmann et al. 2012; Fu et al. 2012, 2013; Bussmann et al. 2013; Messias et al. 2014; Rawle et al. 2014; Bussmann et al. 2015; Timmons et al. 2015).

Wide-area far-infrared surveys have been very successful in detecting lensed SMGs. The steep number counts and the negative k -correction at submillimeter wavelengths give rise to a high magnification bias such that the fraction of lensed sources brighter than a given threshold is significantly larger than other wavelengths (Blain 1996). This has been used by several recent studies (Negrello et al. 2010, 2017; Wardlow et al. 2013; Nayyeri et al. 2016) to identify samples of high-redshift lensed SMGs from *Herschel* observations as well as populations of lensed SMGs from wide-field observations using *Planck* (Cañameras et al. 2015), and in the millimeter band from the South Pole Telescope (Mocanu et al. 2013; Weiß et al. 2013; Mancuso et al. 2016; Strandet et al. 2016) and Atacama Cosmology Telescope (Su et al. 2017).

In this work, we study the physical properties of a *Herschel*-identified SMG at $z = 2.685$ that is lensed by a foreground massive cluster at $z \sim 0.98$ (see Figure 1). The signal boost provided by the gravitational lensing in combination with our high-resolution deep imaging and spectroscopy in the near- and far-infrared gives us a unique opportunity to study the star formation activity and physical properties of this lensed system as a very massive SMG candidate identified during the peak epoch of star formation activity (Madau & Dickinson 2014).

This paper is organized as follows. In Section 2, we describe our photometric and spectroscopic observations of NA.v1.489. In Section 3, we discuss our lens modeling of the system using high-resolution photometric and spectroscopic data of the foreground cluster system. We study the physical properties of the lensed system in Section 4. The results of the combined lens modeling, SED fitting, and spectral line analysis are discussed in Section 5, and in Section 6, we summarize our main findings. Throughout this paper, we assume a standard cosmology with $H_0 = 70 \text{ km s}^{-1} \text{ Mpc}^{-1}$, $\Omega_m = 0.3$, and $\Omega_{\Lambda} = 0.7$. All magnitudes are in the AB system, where $m_{\text{AB}} = 23.9 - 2.5 \times \log(f_{\nu}/1 \mu\text{Jy})$ (Oke & Gunn 1983).

2. Data

2.1. *Herschel* Far-infrared Imaging

H-ATLAS J133542.9+300401 lensed SMG (hereafter referred to as NA.v1.489) was discovered by the *Herschel* Space Observatory (Pilbratt et al. 2010) as part of the Astrophysical Terahertz Large Area Survey (*H-ATLAS*; Eales et al. 2010). The observations were performed with the Spectral and Photometric Imaging REceiver (SPIRE; Griffin et al. 2010) instrument at $250 \mu\text{m}$, $350 \mu\text{m}$, and $500 \mu\text{m}$. NA.v1.489 was discovered as a SPIRE $500 \mu\text{m}$ bright source (with $S_{500} > 100$ mJy) within *H-ATLAS* maps as a potential high- z lensed SMG candidate (Negrello et al. 2017) with follow-up CO observations (described below) revealing the high-redshift nature of the source with $z = 2.685$.

The *Herschel* images are processed with the *Herschel* Interactive Processing Environment (HIPE; Ott 2010) and are available from the *Herschel* Science Archive. For the SPIRE photometry, we used the point source catalog for *H-ATLAS* (Valiante et al. 2016; S. J. Maddox et al. 2017, in preparation), which includes photometry in all three SPIRE bands (at $250 \mu\text{m}$, $350 \mu\text{m}$, and $500 \mu\text{m}$). The PACS and SPIRE images will be released in future studies (M. W. L. Smith et al. 2017, in preparation) along with the source catalogs (S. J. Maddox et al. 2017, in preparation). The details of the object selection and photometry are described in Valiante et al. (2016).

2.2. GBT Spectroscopy of CO ($1 \rightarrow 0$)

The NRAO²⁰ Green Bank Telescope (GBT) was used to carry out the CO ($1 \rightarrow 0$) observations of NA.v1.489 during three observing sessions (2012 November 29 and 30, and 2014 April 05; GBT programs 12A299 and 13A137, PI: D. Frayer). These observations were part of a comprehensive CO ($1 \rightarrow 0$) redshift survey of *H-ATLAS* sources using the Zpectrometer instrument on the GBT (Frayer et al. 2011; Harris et al. 2012). The observations were taken using the subreflector beam switching (“SubBeamNod”) mode with a 10 s switching interval. Alternating sets of SubBeamNod observations between the two targets were taken every 4 minutes to remove the residual baseline structure. A total of 2.7 hr of on-source observations were obtained for NA.v1.489. The data were reduced using the standard Zpectrometer data reduction package (Harris et al. 2012). Based on the dispersion of the measurements of the nearby pointing source, we estimate a 15% absolute calibration uncertainty for the data. Figure 2

²⁰ The National Radio Astronomy Observatory is a facility of the National Science Foundation operated under cooperative agreement by Associated Universities, Inc.

shows the GBT measured velocity at $z = 2.685$ (determined from combined GBT and CARMA observations; see Figure 2 and Section 2.3 below).

2.3. CARMA Spectroscopy of CO (3 \rightarrow 2)

Observations of the CO (3 \rightarrow 2) rotational line ($\nu_{\text{rest}} = 345.8$ GHz) toward the background galaxy NA.v1.489 at $z = 2.685$ were carried out using the Combined Array for Research in Millimeter-wave Astronomy²¹ (CARMA) at the redshifted frequency of $\nu_{\text{obs}} = 93.838$ GHz (3.2 mm; Program ID: cf0020, cf0025; P.I. Riechers). Two observing runs were carried out on 2013 April 27 and June 9 under excellent 3 mm weather conditions in the C and D array configurations, respectively. The 3 mm receivers were used to cover the redshifted CO (3 \rightarrow 2) line, employing a correlator setup providing a bandwidth of 3.75 GHz in each sideband and spectral resolution of 5.208 MHz (~ 17 km s⁻¹). The line was placed in the upper sidebands for both tracks with the local oscillator tuned to $\nu_{\text{LO}} \sim 90.7$ GHz; this resulted in 1.9 and 2.6 hr of 15 antenna-equivalent on-source time after discarding unusable visibility data for the C and D array observations, respectively.

For both tracks, the nearby radio quasar J1310+323 was observed every 15 minutes for pointing, amplitude, and phase calibration, and MWC 349 was observed as the primary absolute flux calibrator. J1337-129 and 3C 273 were observed as bandpass calibrators for the C and D array observations, respectively, yielding $\sim 15\%$ calibration accuracy. The MIRIAD package was used to calibrate and analyze the visibility data, which are imaged and de-convolved using the CLEAN algorithm with “natural” weighting. This yields a synthesized clean beam size of $2''.6 \times 2''.2$ for the upper sideband image cube. The final rms noise is $\sigma = 0.68$ Jy km s⁻¹ beam⁻¹ over a channel width of 208.3 MHz (corresponding to 687 km s⁻¹). The continuum image is created by averaging over all of the line-free channels ($\nu_{\text{cont}} \sim 90.7$ GHz). This yields a synthesized clean beam size of $3''.5 \times 3''.0$ and an rms noise of 0.24 mJy beam⁻¹. These observations ultimately confirm the redshift of NA.v1.489 to be $z = 2.685$, and thus, that the line detected with the GBT indeed is CO (1 \rightarrow 0). They also provide a precise position for the molecular gas reservoir, which is consistent with that subsequently found for the dust emission based on SMA observations (see Section 2.8)

2.4. Hubble Space Telescope WFC3 Imaging

NA.v1.489 was observed with the *Hubble* Space Telescope Wide Field Camera 3 (*HST*/WFC3) F110W filter (at 1.1 μm) in Cycle 19 as part of the SNAP imaging program of *Herschel*-identified lensed SMGs (PID: 12488; PI: Negrello; Negrello et al. 2014). The data were reduced using the IRAF MultiDrizzle package with a resampled pixel scale of $0''.064$ using the adopted dithering pattern (Negrello et al. 2014). The acquired image has an exposure time of 252 s and reaches a 5σ limiting depth of 25.1 AB mag (over a $1''$ aperture). Figure 1 shows the *HST* image along with additional observations.

2.5. Keck Adaptive Optics Imaging

We observed NA.v1.489 in 2015 February 7 and 8, with the Keck/NIRC2 Adaptive Optics (AO) imaged (PID: U038N2L;

PI: Cooray) in the *H*- and *K_s*-band filters at 1.63 μm and 2.15 μm , respectively, with an average seeing of 0.6–0.7 arcsec. The observations are done with a custom nine-point dithering pattern for sky subtraction with 120 and 80 s exposures per frame at 0.04 arcsec pixel⁻¹. We also acquired dark images with the hatch closed and dome flats with and without the calibration lamps. The individual frames are then co-added, and flat and dark subtracted using custom IDL routines. The combined images have exposure times of 5640 and 5280 s in the *H* and *K_s* bands, respectively. A natural guide star of $R = 17.3$ mag with a distance of 52.3 arcsec was used for the tip-tilt correction. Figure 1 shows the *HST* + Keck combined image of the lensed system.

2.6. Keck Optical Spectroscopy

The lensing system was observed with the Keck/DEIMOS optical spectrograph (Faber et al. 2003) on 2015 February 26, (PID:U029D; PI: Cooray). The G1–G4 foreground galaxies (Figure 1) were observed using the DEIMOS Long1.0B, which is a single long slit of width 1 arcsec and consists of 12 slitlets each 82 arcsec long. A P.A. of -37° was chosen to align the galaxies on the slit with a star of $R = 17.5$ mag at an offset of $47''$ and $-29''$ (east and north) with respect to the center of the four lens used as guiding. The foreground system was observed for a total of 1100 s using the 600 lines mm⁻¹ grating with a resolution of 3.5 Å and under clear conditions with ~ 0.6 arcsec seeing. A central wavelength of 6700 Å blazed at 7500 Å was chosen for the observations giving a wavelength coverage of 4050 Å–9350 Å.

The observed spectra were flat fielded and wavelength calibrated using the DEEP2 pipeline. The 1D spectra were extracted at the position of the four galaxies with optimal extraction (Horne 1986). Figure 3 shows the extracted 1D spectra for the four co-aligned galaxies. We detect the [O II] doublet $\lambda 3728$, $\lambda 3729$ emission and/or Ca H&K absorption in the extracted 1D spectra, putting the foreground system at $z \sim 0.98$. This is the redshift that we adopt for our lens modeling.

2.7. JVLA Imaging

The National Radio Astronomy Observatory’s (NRAO’s) JVLA²² observations used in this paper were carried out on 2015 February 15 and 17, when the array was in its B-configuration (PI: R. Ivison, ID: 14B-475). Simultaneous 4 GHz bandwidth in dual polarization covered the 3.9–7.8 GHz range (C band). The calibrator 3C 286 was used for bandpass, phase, and flux calibration. The data were calibrated and imaged in CASA²³ using standard calibration techniques, including automatic RFI flagging. The image has an rms of 7.8 $\mu\text{Jy beam}^{-1}$ with a synthesized beam size of $1''.01 \times 0''.81$ at P.A. = -71.6 deg.

2.8. Submillimeter Array Imaging

NA.v1.489 was initially observed using the Submillimeter Array (SMA; Ho et al. 2004) in 2015 December. Observations were performed on December 1 (2.6 hr on source, with seven antennas) and December 7 (1.86 hr on source with eight

²¹ <http://www.astro.caltech.edu/research/carma/>

²² This work is based on observations carried out with the JVLA. The NRAO is a facility of the NSF operated under cooperative agreement by Associated Universities, Inc.

²³ <https://casa.nrao.edu/>

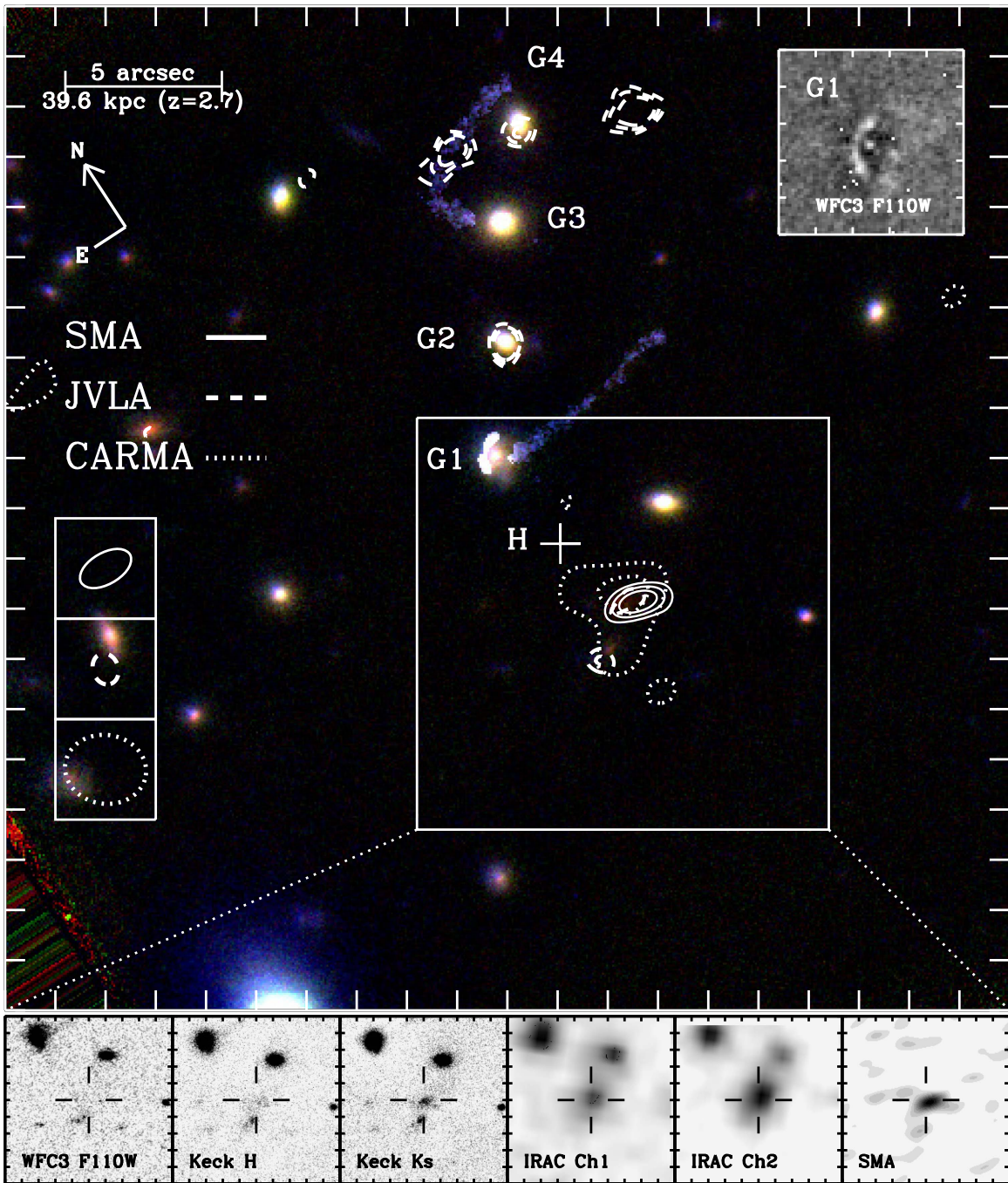


Figure 1. *HST* F110W + Keck NIRC2 *H*- and *K_s*-band three-color image of the NA.v1.489 system along with the four main deflecting galaxy potentials marked G1–G4, which are part of a foreground cluster at $z \sim 0.98$ (Stanford et al. 2014). The solid box center marks the position of the high- z SMG studied here and presented in the subpanel. The JVLA, SMA, and CARMA observations are shown with white contours on the image. The contours are drawn at the 5σ , 7σ , and 9σ levels for JVLA and SMA and at the 3σ , 5σ , and 7σ levels for CARMA ($\sigma_{\text{JVLA}} = 7.8 \mu\text{Jy beam}^{-1}$, $\sigma_{\text{SMA}} = 0.36 \text{ mJy beam}^{-1}$, $\sigma_{\text{CARMA}} = 0.68 \text{ Jy beam}^{-1} \text{ km s}^{-1}$). The *Herschel* centroid is marked with a plus and is consistent with the peak SMA, CARMA, and JVLA emissions given the PSF FWHM size of *Herschel*/SPIRE at $250 \mu\text{m}$ ($\sim 18''$). The top-right box shows the zoomed-in F110W image of G1 revealing a lensed system. This, together with the extended blue arcs (none of which are part of the SMG under study), is used to construct the lens model of the cluster. The radio emissions around G4 are likely radio lobes associated with a Fanaroff-Riley Type II (FR-II) radio source (Fanaroff & Riley 1974), which is also detected in VLA FIRST (Becker et al. 1994) and NVSS (Condon et al. 1998).

antennas) when the array was in its most compact configuration. The array was tuned to a local oscillator (LO) frequency of 228.3 GHz ($\lambda = 1.31 \text{ mm}$), and the integrated bandwidth was 6.25 GHz per sideband (12.5 GHz total bandwidth). Both observations were obtained in good weather, and emission was detected at $5.00 \pm 0.54 \text{ mJy}$, located roughly $11''$ from the phase center.

Given the strong detection, further observations in the compact ($\sim 70 \text{ m}$ max baseline for 2.8 hr on 2016 January 22) and extended ($\sim 220 \text{ m}$ max baseline for 5.2 hr on 2016 April 14) SMA configurations were obtained. The LO tuning was again 228.3 GHz, with $\sim 7 \text{ GHz}$ bandwidth per sideband utilized (14 GHz total bandwidth). Phase and amplitude gain calibration was performed using the nearby sources J1310+323

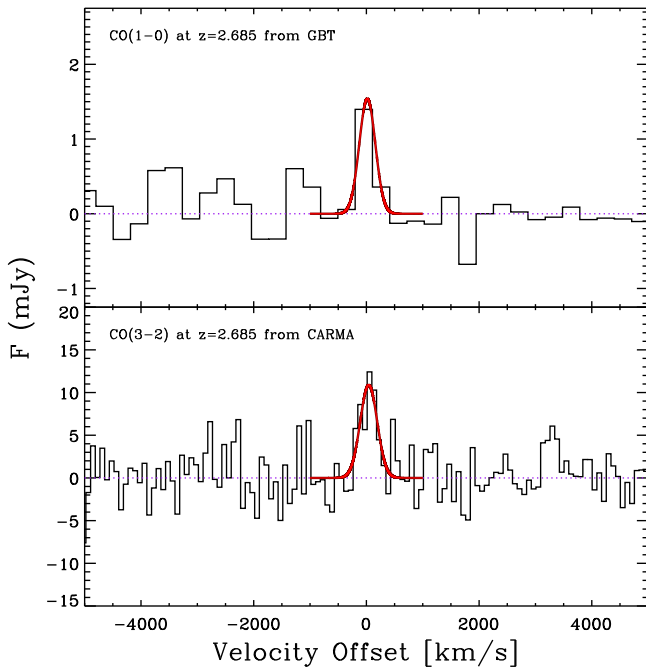


Figure 2. CO ($1 \rightarrow 0$) from GBT (top) and CO($3 \rightarrow 2$) detection at $z = 2.685$ from CARMA (bottom) for NA.v1.489. The red curves show the best-fit Gaussian to the lines centered on $v = 0$ at $z = 2.685$ for the 31.3 GHz and 93.8 GHz emission lines from GBT and CARMA. The best fits have FWHM ($=2\sqrt{2\ln 2} \sigma$) of $305 \pm 87 \text{ km s}^{-1}$ and $351 \pm 25 \text{ km s}^{-1}$, and peak flux of 1.54 mJy and 10.95 mJy for the CO ($1 \rightarrow 0$) and CO($3 \rightarrow 2$) emissions respectively.

and 3C 286, with passband calibration performed using 3C 279, and the flux density scale set using Callisto, known to 5% at 1.3 mm. Both observations were obtained under very good weather (225 GHz opacities of 0.07 in January and 0.04 in April). The observations were calibrated and ported into the NRAO Astronomy Image Processing System (AIPS). These are the data we use in this study.

Direct fitting of the visibility data determined that the emission is best fit by a Gaussian with a peak of $5.93 \pm 0.43 \text{ mJy}$, offset from the phase center by $+1''.9 \text{ R.A.}$, $-11''.1 \text{ decl.}$, matching the integrated flux and position determined at low resolution, and further suggesting a characteristic size of $0''.9 \text{ FWHM}$. The data were also imaged, confirming again the positional offset and flux density. The synthesized beam of the combined observations was $1''.8 \times 1''.0$.

2.9. Archival Data

The lensing cluster has been observed by the Gemini-North GMOS in both imaging and spectroscopy modes (MOO J1335 +3004; Stanford et al. 2014). The imaging observations are in the r and z bands (at 6300 Å and 9250 Å) with total exposure times of 900 and 2160 s, respectively (Stanford et al. 2014), and spectroscopic observations of candidates identified from the optical catalogs with total on-source exposure time of 6480 s. NA.v1.489 is not detected in these Gemini observations. We use this spectroscopic and imaging data set to identify the foreground lensing galaxies and distorted images associated with the lensing cluster as discussed in the next section.

The foreground cluster was observed by *Spitzer*/IRAC at 3.6 μm and 4.5 μm in Cycle 12 in the warm mission (PI: A. Gonzalez) and separately by the *Wide-field Infrared Survey Explorer* (*WISE*; Wright et al. 2010) in all four W1, W2, W3,

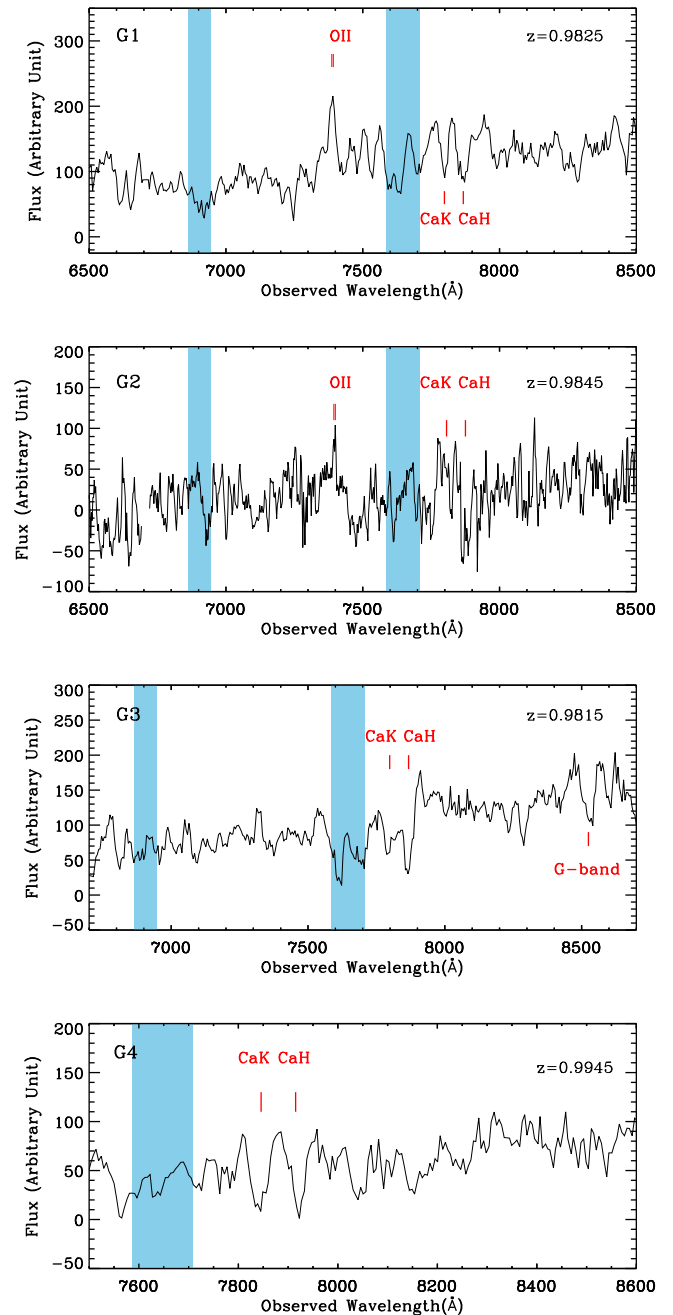


Figure 3. Keck/DEIMOS 1D spectra of the foreground lensing galaxies extracted from the 2D spectra at the position of G1–G4 (Figure 1). The main atmospheric contaminations in the wavelength range are marked as blue shaded regions. All four galaxies have spectroscopic redshifts measured from the [O II] ($\lambda 3728$, $\lambda 3729$) emission and/or Ca K ($\lambda 3934$) and Ca H ($\lambda 3968$) absorption putting them at $z = 0.98\text{--}0.99$, consistent with the previous spectroscopic measurements for the other cluster members in the field from GMOS on Gemini (Stanford et al. 2014).

and W4 bands. The IRAC observations were done with 30 s exposures in both bands. The IRAC mosaics were in MJy sr^{-1} , which were converted to $\mu\text{Jy pixel}^{-1}$ using a pixel scale of 0.6 arcsec. NA.v1.489 is detected in both IRAC bands with at least $S/N \sim 9$.

2.10. Multiband Photometry

We measured the photometry of the background SMG using SEXTRACTOR (Bertin & Arnouts 1996). The zero points for the

Table 1
Observed Photometric Data for NA.v1.489 (R.A.^a:13^h35^m42^s.8,
Decl.^a:+30°03′58″.1) at $z = 2.685$

Instrument	Flux Density
<i>HST</i> /WFC3 F110W	$1.16 \pm 0.39 \mu\text{Jy}$
Keck <i>H</i>	$7.30 \pm 2.37 \mu\text{Jy}$
Keck K_s	$18.06 \pm 4.07 \mu\text{Jy}$
<i>Spitzer</i> /IRAC 3.6 μm	$67.18 \pm 7.10 \mu\text{Jy}$
<i>Spitzer</i> /IRAC 4.5 μm	$93.36 \pm 5.41 \mu\text{Jy}$
<i>WISE</i> W3	$115.0 \pm 16.0 \mu\text{Jy}$
<i>WISE</i> W4	$911.3 \pm 190.4 \mu\text{Jy}$
<i>Herschel</i> /SPIRE 250 μm	$136.6 \pm 7.2 \text{ mJy}$
<i>Herschel</i> /SPIRE 350 μm	$145.7 \pm 8.0 \text{ mJy}$
<i>Herschel</i> /SPIRE 500 μm	$125.0 \pm 8.5 \text{ mJy}$
SMA 1.31 mm	$5.93 \pm 0.43 \text{ mJy}$
CO(3 \rightarrow 2) 3.2 mm Cont.	$874.6 \pm 55 \mu\text{Jy}$
JVLA 1.4 GHz ^b	$134.9 \pm 21.8 \mu\text{Jy}$

Notes.

^a From peak SMA.

^b From JVLA 6.89 GHz observations assuming a spectral index of $\alpha = -0.8$.

Keck observations were computed by comparing the photometry of the bright targets in the field to those in the UKIRT Infrared Deep Sky Survey (UKIDSS; Lawrence et al. 2007). We run SEXTRACTOR in dual mode with the Keck K_s image as the detection band for the *HST* and Keck photometry.

For the IRAC observations, we use each band as its own detection when running SEXTRACTOR. We measure the *WISE* flux density of NA.v1.489 through aperture photometry with $r_{\text{ap}} = \text{PSF FWHM}$ in each band centered on the *Spitzer*/IRAC 3.6 μm centroid. *WISE* aperture photometry overestimates the fluxes in the W1 and W2 bands compared to the IRAC 3.6 μm and 4.5 μm observations by $\sim 29\%$ due to blending. We corrected the *WISE* W3 and W4 fluxes with the same factor to account for blending.

Herschel/SPIRE photometry, as discussed above, is from the *H-ATLAS* catalog of Valiante et al. (2016). For the longer wavelength SMA and JVLA, we first convert the maps from Jy beam⁻¹ units to mJy pixel⁻¹ given the beam size of the observations and the data pixel scale and perform photometry on each image individually. Table 1 summarizes the photometry extracted for the background SMG. We use this multiband photometry to construct the SED of the lensed galaxy in Section 4.

3. Lensing Model

The NA.v1.489 system is gravitationally lensed by a foreground cluster of galaxies at $z = 0.98$ first identified in the *WISE* survey by Stanford et al. (2014) with follow-up spectroscopic and photometric observations with Gemini as discussed above. The extended arcs associated with lensing (of a galaxy at an unknown redshift) are visible in the high-resolution *HST* image of the cluster (blue arcs in Figure 1). The SMG (marked in Figure 1 with the solid box) was independently identified from *Herschel* 500 μm observations by Negrello et al. (2017) as a potential lensed candidate. We performed lens modeling of this system using the publicly available code of LENSTOOL²⁴ (Kneib et al. 1996; Jullo et al. 2007; Jullo & Kneib 2009). LENSTOOL performs Bayesian

optimization given the redshift and location of the identified images of the lensed sources in the image plane. We used the two blue extended arcs identified in the G1–G4 system (Figure 1) along with the arc produced by G1 to constrain the lens model. We used SEXTRACTOR on the Gemini *r*-band to identify the peak positions of the arcs and counter images in the image plane as required by LENSTOOL. We allowed the redshift of the arcs to vary during the optimization. In the lens modeling analysis, we used a combination of a cluster potential together with galaxy potentials as the foreground deflecting components. We use an NFW profile (Navarro et al. 1996) for the lensing cluster at $z = 0.98$ consistent with the spectroscopic observations of various cluster members. For the galaxy-scale potentials, we used the spectroscopic identifications from Gemini (Stanford et al. 2014) and our Keck/DEIMOS observations as the main foreground system combined with red-sequence-identified cluster members from the color–magnitude diagram from the Gemini+*HST* extracted photometry. Figure 4 shows the foreground potentials used to construct the lensing system. We additionally keep the cluster potential ellipticity and position variable, with the allowed centroid offset of 10 arcsec around the initial value (at the center of the four galaxies).

The output of the optimization process provides the best estimate positions and properties of the deflecting potentials and is considered the best-fit model. Figure 4 shows the best-fit model computed by LENSTOOL along with the generated amplification map. We use this map to measure the magnification of the SMG at the SMA peak position. Averaging the amplification map across the corresponding images identified from the SEXTRACTOR segmentation maps yield magnifications of $\mu_{\text{star}} = 2.10 \pm 0.11$ and $\mu_{\text{dust}} = 2.02 \pm 0.06$ for the stellar and dust components, respectively, from the modes of the computed Bayesian model. We note here that the magnifications for both emissions (stellar and dust) are computed from the same amplification map (constructed from the Gemini *r*-band) for the lensing cluster due to the lack of multiple images associated with dust that would allow a separate lens modeling. In the next section, we de-magnify the stellar and dust continuum fluxes by the above-measured values before measuring the physical properties through SED fitting.

Figure 5 shows the Gemini *r*-band image used in lens modeling along with the reconstructed lens model in the image plane and the residual map. The reconstructed image is generated by tracing the source plane image through the best-fit lens model. We further show the source plane reconstruction of the blue arcs used in generating the model in this figure for reference. Figure 6 shows the Keck and SMA images of the lensed SMG NA.v1.489, along with the source plane reconstructed three-color image using the lens model computed for the cluster as discussed above. The reconstructed source plane has red colors as expected from the observed SED and consistent with other rest-frame optical studies of SMGs. The rest-frame optical emission, as arising from stellar light, has a co-moving distance of ~ 0.6 kpc from SMA dust emission in the source plane. The stellar and dust emissions have half-light radii of 0.63 kpc and 1.86 kpc, respectively, measured from a Sérsic profile using GALFIT (Peng et al. 2002). This shows a more extended dust emission that is also offset from the stellar light as reported previously in the literature for high- z SMGs (Hodge et al. 2015; Spilker et al. 2015) and would suggest the

²⁴ <http://projets.lam.fr/projects/lenstool/wiki>

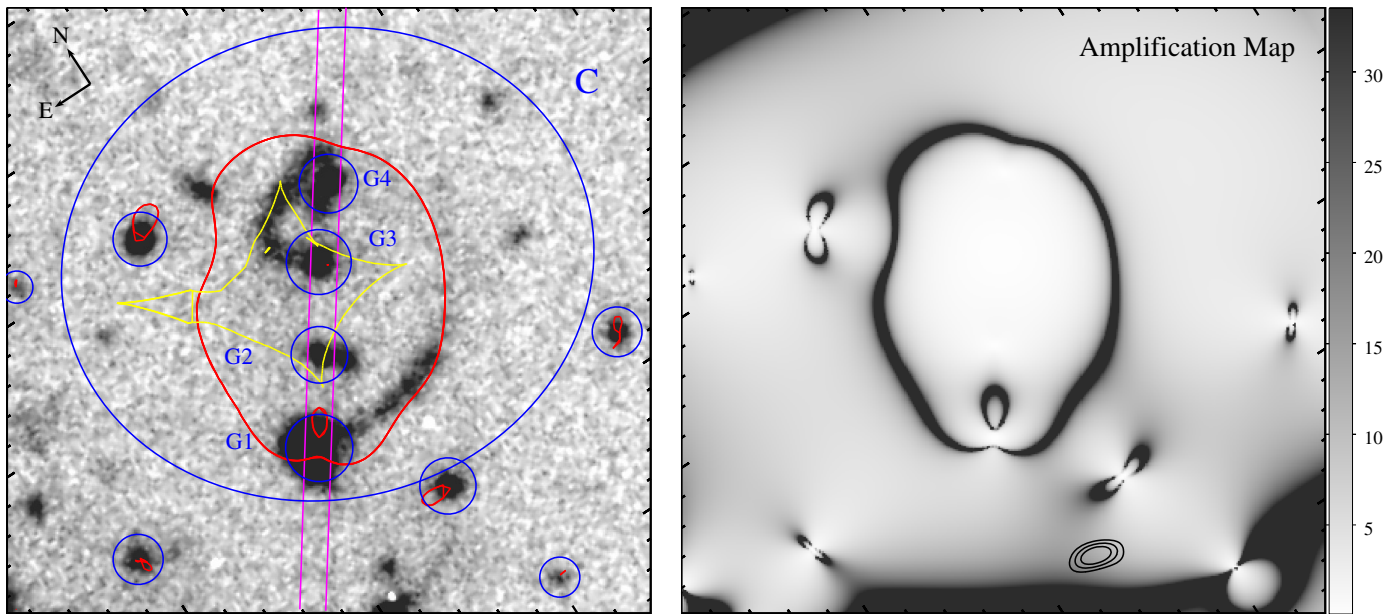


Figure 4. Left: the Gemini r -band image of the foreground cluster lensing system. The blue lines show the foreground potentials at $z \sim 1$ used to construct the lens model, which includes the main cluster potential (marked with C) and the galaxy potentials, including the four main galaxies marked G1–G4 (see Figure 1), identified from spectroscopic observations by Gemini (Stanford et al. 2014) and our own Keck/DEIMOS observations (Keck long-slit shown in magenta). The red and yellow curves show the critical and caustic lines associated with the best-fit model. Right: the amplification map of the best-fit lens model. The source magnification is estimated by averaging this map across the object image area identified from the SEXTRACTOR segmentation maps. The black contours are from SMA observations of NA.v1.489 (at the 5σ , 7σ , and 9σ levels; see Figure 1).

presence of differential magnification (yet not significant) as reported above for the stellar and dust components.

4. Physical Properties of NA.v1.489

4.1. SED-inferred Parameters

We fit the SED of the background SMG with a library of model templates using the publicly available SED-fitting code MAGPHYS (da Cunha et al. 2008). MAGPHYS uses the Bruzual & Charlot (2003) synthesis models for the stellar light and the attenuation by Charlot & Fall (2000) to compute the total infrared luminosity absorbed and re-radiated by dust using different dust components at different wavelengths based on an energy balance scheme (da Cunha et al. 2008). We used an updated version of the MAGPHYS code that is better suited for $z > 1$ SMGs (da Cunha et al. 2015). Briefly, it does so by extending the SED parameter priors to the high-redshift, high optical depth, and actively star-forming regime that is typical of star-forming galaxies at high redshift by adding new star formation histories and dust attenuation recipes (da Cunha et al. 2015).

We use the photometry of NA.v1.489 outlined in Table 1 and correct it for the magnification (reported in the previous section) as an input for SED fitting in MAGPHYS. This includes near-infrared data from *HST*/WFC3 F110W; Keck H and K_s , infrared measurements by *Spitzer*/IRAC in $3.6 \mu\text{m}$ and $4.5 \mu\text{m}$; *WISE* observations at $12.0 \mu\text{m}$ and $22.0 \mu\text{m}$; far-infrared photometry from *Herschel*/SPIRE in the $250 \mu\text{m}$, $350 \mu\text{m}$, and $500 \mu\text{m}$ bands; and 1.31 mm observations by SMA. For the SED fitting, we fixed the redshift of the galaxy to its spectroscopic redshift ($z = 2.685$) measured from CO observations. The best-fit SED and photometry are presented in Figure 7 with the best-fit measured physical parameters reported in Table 2. For the star formation rate, we used a Kennicutt relation (Kennicutt 1998) with a Chabrier initial

mass function (Chabrier 2003) to convert the total infrared luminosities to SFR ($\text{SFR} = 1 \times 10^{-10} L_{\text{IR}}$; Riechers et al. 2013). The SED of NA.v1.489 is consistent with the presence of a Balmer break at $z \sim 2.6$ and would allow for robust stellar mass estimates.

It is important to note that the SED-inferred parameters are for stellar light heating the dust and does not include the AGN contribution. NA.v1.489 shows excess radio flux with respect to the infrared luminosity compared to the average values expected for high- z SMGs, which could hint at the presence of an AGN. Although there are studies such as that by Wang et al. (2013), which shows a low fraction of AGN presence within SMG populations, there are studies that point to the existence of an AGN component within SMGs (Wang et al. 2013).

The lack of an AGN recipe in our SED fitting with MAGPHYS should not strongly affect the estimated physical parameters (da Cunha et al. 2015). In a recent study, in fact, using synthetic models of galaxies with *H-ATLAS*-like photometry computed from simulations, Hayward & Smith (2015) showed that MAGPHYS-estimated physical properties are robust even in the extreme case of an AGN contributing as much as 25% to UV to IR luminosity.

Physical properties measured from SED fits have inherent uncertainties associated with the choices of the input parameters in building the templates, such as the assumed star formation history and dust attenuation (Conroy 2013). To further examine the robustness of our estimated physical properties, and in particular the stellar mass, we applied the SED-fitting method detailed in Michałowski et al. (2008, 2009, 2010b, 2010c, 2012, 2014), which is based on 35,000 templates from the library of Iglesias-Páramo et al. (2007) plus some templates of Silva et al. (1998) and Michałowski et al. (2008), all of which were developed using GRASIL²⁵

²⁵ <http://adlibitum.oats.inaf.it/silva/grasil/grasil.html>

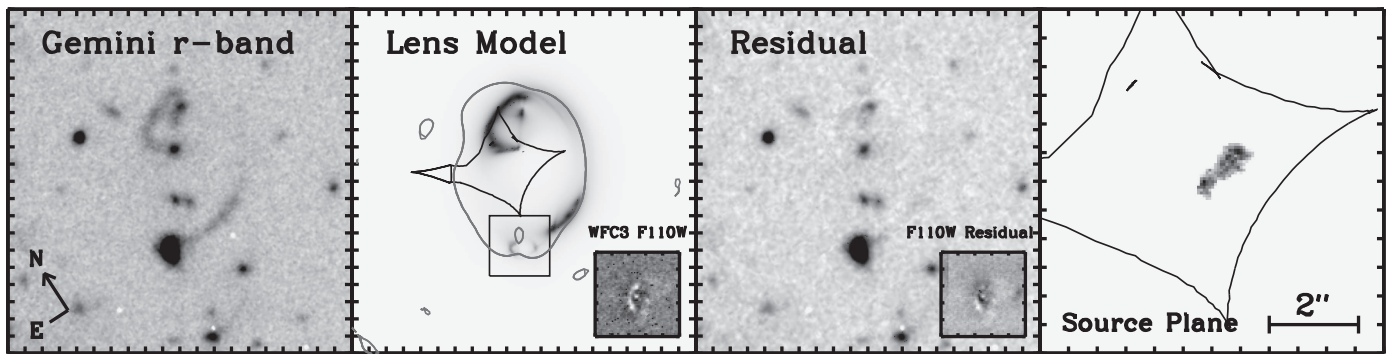


Figure 5. Lens model of the foreground cluster constructed by LENSTOOL using the Gemini *r*-band image. The lens panel further shows the critical and caustic lines constructed by the model. The subpanels in the lens model and residual maps represent the F110W image and the residual of the small arc around G1, respectively. The source plane reconstruction of the blue arcs (Figure 1) in the cluster field used for building the model is shown in the far right.

(Silva et al. 1998). They are based on numerical calculations of radiative transfer within a galaxy, which is assumed to be a triaxial axisymmetric system with diffuse dust and dense molecular clouds, in which stars are born. The templates cover a broad range of galaxy properties from quiescent to starburst, and span an A_V range from 0 to 5.5 mag. The extinction curve (Figure 3 of Silva et al. 1998) is derived from the modified dust grain size distribution of Draine & Lee (1984). The star formation histories are assumed to be a smooth Schmidt-type law, i.e., the SFR is proportional to the gas mass to some power (see Silva et al. 1998), with a starburst (if any) on top of that, starting 50 Myr before the time at which the SED is computed. There are seven free parameters in the library of Iglesias-Páramo et al. (2007): the normalization of the Schmidt-type law, the timescale of the mass infall, the intensity of the starburst, the timescale for molecular cloud destruction, the optical depth of the molecular clouds, the age of the galaxy, and the inclination of the disk with respect to the observer. Michałowski et al. (2012, 2014) found that the choice of star formation history (SFH) assumed in the SED modeling can lead to a systematic shift of stellar mass. However, this shift is at most a factor of ~ 2 for a single-burst SFH (i.e., all stars formed at the same epoch), unrealistic for such a massive and actively star-forming galaxy. Moreover, double-component SFHs (utilized here) were found to result in the most accurate stellar masses of real (Michałowski et al. 2012) and simulated SMGs (Michałowski et al. 2014; Hayward & Smith 2015). We re-fit our observed SED with the new set of templates using GRASIL as discussed above. Figure 7 shows the GRASIL best-fit template compared to that of MAGPHYS. Our newly measured physical properties, and stellar mass, from the new templates are consistent with our original measurements using MAGPHYS.

4.2. Molecular Gas and Dust

We use the velocity-integrated CO flux ($S_{\text{CO}} \Delta v$), measured from GBT observations (Figure 2), to estimate the CO line luminosity given the spectroscopic redshift of the SMG. The best-fit Gaussian to CO ($1 \rightarrow 0$) at 31.28 GHz yields a peak observed flux of 1.54 mJy and a velocity FWHM of $305 \pm 87 \text{ km s}^{-1}$. The CO line luminosities could be calculated as (Solomon & Vanden Bout 2005; Ivison et al. 2011; Bolatto

et al. 2013; Carilli & Walter 2013; Scoville et al. 2016):

$$L'_{\text{CO}} [\text{K km s}^{-1} \text{ pc}^2] = 3.25 \times 10^7 (S \Delta v [\text{Jy km s}^{-1}]) \times (\nu_{\text{obs}} [\text{GHz}])^{-2} (D_L [\text{Mpc}])^2 \times (1+z)^{-3} \quad (1)$$

This yields a magnification-corrected CO ($1 \rightarrow 0$) line luminosity of $L'_{\text{CO}(1 \rightarrow 0)} = 1.04 \pm 0.12 \times 10^{11} \text{ K km s}^{-1} \text{ pc}^2$. Assuming a $L'_{\text{CO}} - M(\text{H}_2)$ conversion factor of $\alpha_{\text{CO}} = 0.8 M_{\odot} (\text{K km s}^{-1} \text{ pc}^2)^{-1}$, which is commonly adopted for starbursting galaxies (Downes & Solomon 1998; Solomon & Vanden Bout 2005; Tacconi et al. 2008), we measure a molecular gas mass ($M(\text{H}_2) = \alpha_{\text{CO}} L'_{\text{CO}}$) of $8.32 \pm 0.09 \times 10^{10} M_{\odot}$ for NA.v1.489.

The CO ($3 \rightarrow 2$) observations obtained with CARMA yield a magnification-corrected line luminosity of $L'_{\text{CO}(3 \rightarrow 2)} = 7.30 \pm 0.12 \times 10^{10} \text{ K km s}^{-1} \text{ pc}^2$. This yields a line ratio of $r_{32/10} = L'_{\text{CO}(3 \rightarrow 2)} / L'_{\text{CO}(1 \rightarrow 0)} = 0.70 \pm 0.16$. This is similar to the line ratios derived from large samples of SMGs at $z \sim 2$ with $r_{32/10} = 0.78 \pm 0.27$ (Sharon et al. 2016).

The ISM mass can also be estimated from submillimeter continuum emission (Magdis et al. 2012; Scoville et al. 2014, 2016) as the dust emission is optically thin at long wavelengths. Scoville et al. (2016) provide an empirical calibration to measure the ISM from the Rayleigh-Jeans tail emission at $850 \mu\text{m}$:

$$M_{\text{ISM}} = 1.78 \times S_{\nu}^{\text{obs}} [\text{mJy}] \times (1+z)^{-4.8} \times \left(\frac{\nu_{850}}{\nu_{\text{obs}}} \right)^{3.8} (D_L [\text{Gpc}])^2 \times \left\{ \frac{6.7 \times 10^{19}}{\alpha_{850}} \right\} \frac{\Gamma_0}{\Gamma_{\text{RJ}}} \times 10^{10} M_{\odot}, \quad (2)$$

where Γ_{RJ} is the correction applied for deviations from the ν^2 behavior in the RJ tail as defined in Scoville et al. (2014, 2016). We used the SMA observations at 1.31 mm and measured a magnification-corrected ISM mass of $7.92 \times 10^{10} M_{\odot}$. This is consistent with the molecular gas mass estimates derived independently from GBT. From CO observations, we measure a gas depletion timescale ($t_{\text{dep}} \equiv M_{\text{gas}}/\text{SFR}$) of 43 Myr, indicating a rapid phase of star formation, which is also observed in other high-redshift SMGs and starbursts (Tacconi et al. 2008; Messias et al. 2014; Oteo et al. 2016).

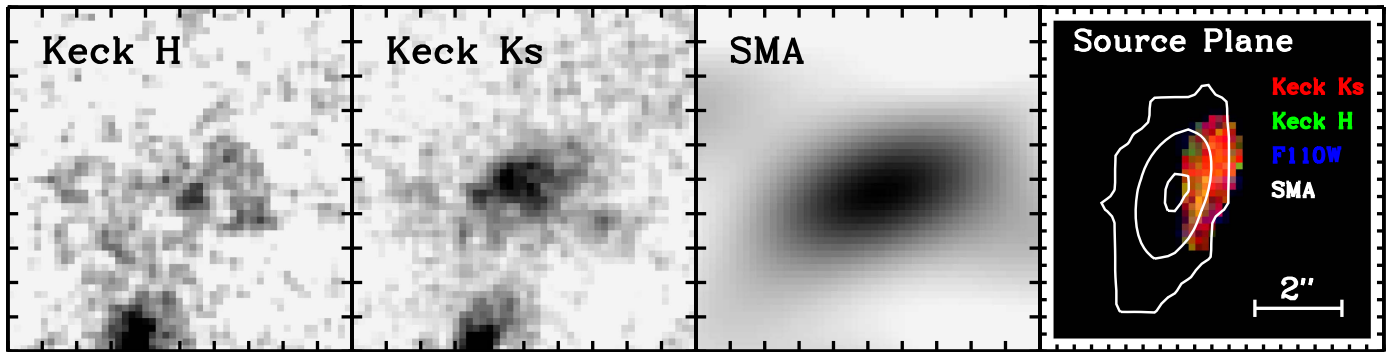


Figure 6. Observed Keck H - and K_s -band images of NA.v1.489 along with the SMA 1.31 mm observations. The right panel shows the combined three-color source reconstructed image along with the SMA contours.

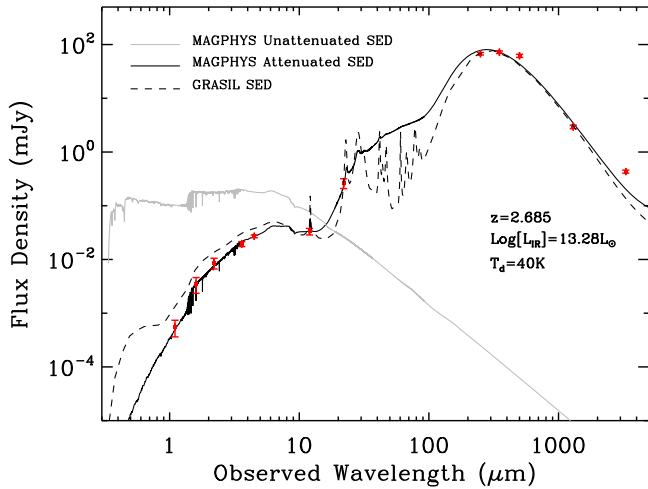


Figure 7. Best-fit SED of the de-magnified flux density of NA.v1.489 using MAGPHYS (da Cunha et al. 2008). During the fitting process, the redshift is fixed to the spectroscopic redshift measured from CO observations. The fit uses photometry from *HST*/WFC3 in the F110W band along with our Keck/NIRC2 observations in the H and K_s bands. The infrared data is from *Spitzer* IRAC observations in the 3.6 μm and 4.5 μm , and *WISE* W3 and W4 bands at 12.0 μm and 22.0 μm respectively. The far-infrared data is from *Herschel*/SPIRE observations in the 250 μm , 350 μm , and 500 μm bands from which the lensing system is originally identified. We also use the SMA 1.31 mm observations in the SED fitting. These data are shown with the red points on top of the best-fit SED (black line) with the unattenuated SED plotted in gray. The best-fit SED yields a total infrared luminosity of $1.9 \times 10^{13} L_{\odot}$.

Table 2
Measured Physical Properties of NA.v1.489

Quantity	Value	Unit
M_*	$6.8^{+0.9}_{-2.7} \times 10^{11}$	M_{\odot}
L_{IR}	$1.9 \pm 0.2 \times 10^{13}$	L_{\odot}
T_d	40 ± 1	K
M_d	$1.5 \pm 0.3 \times 10^9$	M_{\odot}
SFR ^a	1914 ± 180	$M_{\odot} \text{ yr}^{-1}$
$L'_{\text{CO}}{}^b$	$1.0 \pm 0.1 \times 10^{11}$	$\text{K km s}^{-1} \text{ pc}^2$
$M_{\text{gas}}{}^b$	$8.3 \pm 1.0 \times 10^{10}$	M_{\odot}
$L_{\text{IR}}/L'_{\text{CO}}$	184	$L_{\odot} (\text{K km s}^{-1} \text{ pc}^2)^{-1}$

Notes.

^a Assuming a Chabrier initial mass function and a conversion of $\text{SFR}[M_{\odot} \text{ yr}^{-1}] = 1.0 \times 10^{-10} L_{\text{IR}}[L_{\odot}]$ (Riechers et al. 2013).

^b From GBT CO(1 \rightarrow 0) observations corrected for magnification assuming a $L'_{\text{CO}} - M(\text{H}_2)$ conversion factor of $\alpha_{\text{CO}} = 0.8 M_{\odot} (\text{K km s}^{-1} \text{ pc}^2)^{-1}$.

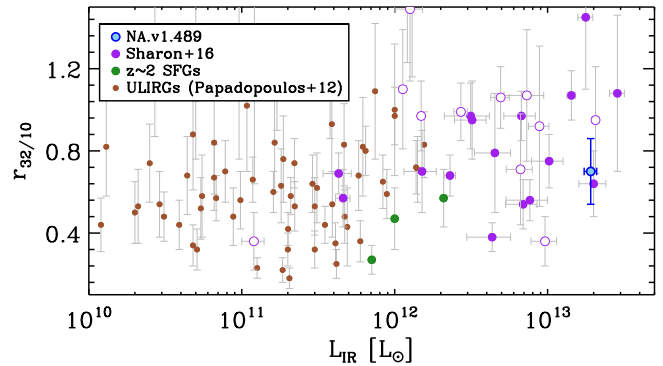


Figure 8. Molecular line intensity ratio of NA.v1.489 ($r_{32/10} = L'_{\text{CO}(3 \rightarrow 2)} / L'_{\text{CO}(1 \rightarrow 0)}$) as measured by GBT and CARMA. The plot shows the same relation for local ULIRGs from Papadopoulos et al. (2012; in brown), $z \sim 2$ SMGs and quasars (Sharon et al. 2016; in magenta), and massive star-forming galaxies (Aravena et al. 2014; Daddi et al. 2015; in green). The $z \sim 2$ SMGs (filled magenta) have average line ratios of $r_{32/10} = 0.78$ while the AGN host galaxies (open magenta) have average measured line ratios of $r_{32/10} = 1.03$ (Sharon et al. 2016), where the $J_{\text{upper}} = 3$ line flux is boosted by emission from the AGN.

5. Discussion

NA.v1.489 has a molecular gas line ratio of $r_{32/10} = 0.70 \pm 0.16$ as measured from GBT and CARMA. This is higher than the measured ratio for normal star-forming galaxies (Aravena et al. 2014; Daddi et al. 2015), with $r_{32/10} = 0.42 \pm 0.07$ (Daddi et al. 2015). The larger value is associated with the increased star formation activity, which could raise the higher- J CO line fluxes at higher energies (Bolatto et al. 2013). The measured molecular gas line flux ratio of NA.v1.489 further agrees with the mean value reported by Sharon et al. (2016) for SMGs (0.78 ± 0.27) at $z \sim 2$. Figure 8 shows the CO molecular line flux ratios as a function of infrared luminosity for NA.v1.489 compared to other SMGs and QSO host galaxies at $z \sim 2$ (Sharon et al. 2016), normal star-forming galaxies (Aravena et al. 2014; Daddi et al. 2015), and local ULIRGs (Papadopoulos et al. 2012). Although the excitation temperature of CO (3 \rightarrow 2) is not very high and could well be produced by a compact starburst (Sharon et al. 2016), a particularly energetic source, such as an AGN, could further increase the $r_{32/10}$ line ratios. NA.v1.489 has measured line ratios consistent with the line excitation produced by a starburst rather than a QSO host galaxy (which has $r_{32/10} = 1.03 \pm 0.50$; Sharon et al. 2016). However, given the uncertainties in both measurements, line excitation due to the presence of an AGN cannot be ruled out.

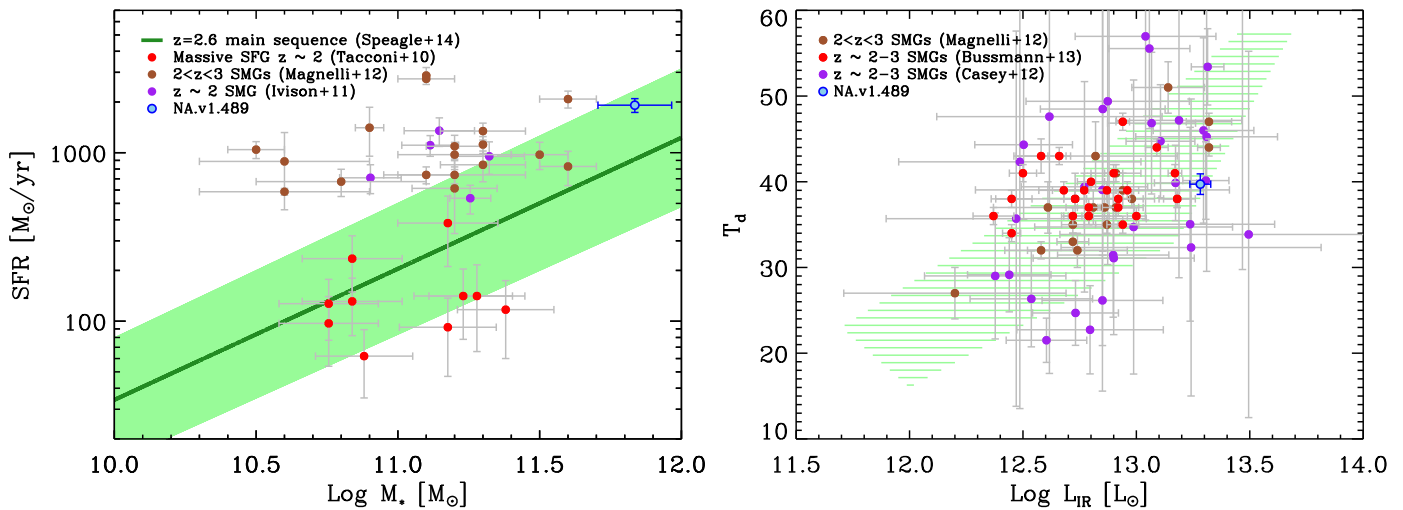


Figure 9. Left: the main sequence of star formation. The green line shows the expected trend for $z = 2.6$ star-forming galaxies reported by Speagle et al. (2014). NA.v1.489 is marked with the blue circle as a massive SMG at $z \sim 2.6$ along with SMGs (Ivison et al. 2011; Magnelli et al. 2012) and massive star-forming galaxies (Tacconi et al. 2010) at similar redshifts. Right: the dust temperature and bolometric infrared luminosity of SMGs (Casey et al. 2012; Magnelli et al. 2012; Bussmann et al. 2013). The green shaded area is the measured locus of SMGs from Chapman et al. (2005). The scatter around the relation is associated with selection biases (Wardlow et al. 2011; Magnelli et al. 2012). NA.v1.489 has a colder dust temperature compared to SMGs at similar redshift, disfavoring a major merger scenario.

NA.v1.489 has an SED-inferred infrared luminosity that puts it among the most IR-luminous extragalactic sources and which then yields an SED-inferred SFR comparable to the most intense star-forming systems at $z \sim 2-3$ (Greve et al. 2005; Fu et al. 2012, 2013; Harris et al. 2012; Magnelli et al. 2012; Ivison et al. 2013). Figure 9 shows the SFR versus stellar mass plot along with the main sequence of star-forming galaxies (Kauffmann et al. 2003; Noeske et al. 2007; Elbaz et al. 2011; Shivaei et al. 2015) derived from Speagle et al. (2014). The $z = 2.6$ main-sequence relation sits above the corresponding local relation such that at any given fixed stellar mass, the high- z counterpart would be much more star-forming compared to the local SFGs. The scatter along this relation, marked as the green shaded area, is associated with the intrinsic properties of galaxies such as the change in star formation histories and metallicities (Brinchmann et al. 2004; Mannucci et al. 2010; Wuyts et al. 2011). As we see from Figure 9, NA.v1.489 sits at the main-sequence relation plotted for $z = 2.6$ from Speagle et al. (2014). This is supported by recent studies of high-redshift SMGs pointing toward small deviations from the SFG main sequence (Michałowski et al. 2012; Koprowski et al. 2014, 2016). The intense SFR agrees with the MS position given the large stellar mass of the system and the huge reservoirs of molecular gas available. The large stellar mass is in agreement with simulations of $z \sim 2$ SMGs (Davé et al. 2010) and SMG models of Hayward et al. (2011) requiring large stellar masses for bright flux densities in the submillimeter (with $M_* > 6 \times 10^{10}$ needed to create an $850 \mu\text{m}$ flux density of 3 mJy) also seen in observed stellar mass estimates of SMGs at $z \sim 2$ from multiwavelength SED measurements (Michałowski et al. 2010a; Hainline et al. 2011). The intense SFR could be explained as being due to the higher molecular gas mass available within these systems that provide the material needed for the excess star formation (Riechers et al. 2010; Fu et al. 2013; Riechers et al. 2014). The dust temperature of SMGs derived from far-IR observations is indicative of the ISM in these systems. The local infrared-luminous SMGs show a clear trend between the dust temperature (T_d) and the infrared luminosity (Hwang et al. 2010; Elbaz et al. 2011; Symeonidis et al. 2013) with similar

trends observed for high-redshift far-infrared or submillimeter-selected samples of galaxies (Chapman et al. 2005; Magdis et al. 2010; Casey et al. 2012; Magnelli et al. 2012, 2014; Béthermin et al. 2015). At high redshift, these relations are biased toward colder temperatures for submillimeter-selected samples at low L_{IR} (Casey et al. 2009; Magnelli et al. 2012) as direct observations in the far-infrared are mostly limited to bright sources at $z \sim 2$ (Magdis et al. 2010) with studies of far-infrared lensed systems extending this to lower L_{IR} (Bussmann et al. 2013; Nayyeri et al. 2016). The T_d-L_{IR} relation shows a modest evolution with redshift from *Herschel*-selected samples out to $z \sim 2-3$ (Hwang et al. 2010), where SMGs at high- z are found to be on average 2–5 K colder than the local counterparts (Hwang et al. 2010). Figure 9 shows that NA.v1.489 has a dust temperature ($T_d = 40$ K) and far-IR luminosity ($L_{\text{IR}} = 1.9 \times 10^{13} L_{\odot}$) that agree with the general trend observed for SMGs (Chapman et al. 2005). The scatter in this relation is associated with selection biases as well as the presence of colder dust temperatures in high- z SMGs (compared to the local counterparts; Magnelli et al. 2012). Figure 9 further shows that NA.v1.489 on average has a colder dust temperature compared to submillimeter- and *Herschel*-selected samples of SMGs at $z \sim 2-3$ at similar infrared luminosities (Casey et al. 2012; Magnelli et al. 2012). The lower dust temperature measured for NA.v1.489 disfavors a major merger scenario. Furthermore, the colder T_d is consistent with a more extended dust distribution (Hwang et al. 2010) as observed from our SMA observations.

The large molecular gas measured from CO observations is responsible for the intense star formation observed in NA.v1.489. Similar reservoirs of cold molecular gas are observed in other extreme starbursts at high redshift (Riechers et al. 2011b, 2013; Fu et al. 2013; Spilker et al. 2015). NA.v1.489 has a gas depletion timescale of ($t_{\text{dep}} \equiv M_{\text{gas}}/\text{SFR}$) 43 Myr, much shorter than the star-forming galaxies ~ 1 Gyr at similar redshifts (Genzel et al. 2010; Decarli et al. 2016a, 2016b) and comparable to gas depletion timescales in other submillimeter-selected dusty galaxies at high redshift (Riechers et al. 2010, 2013). The short timescale and intense star formation rates are responsible for the mass build-up in NA.v1.489. Figure 10 shows the gas depletion timescale of NA.v1.489 compared to

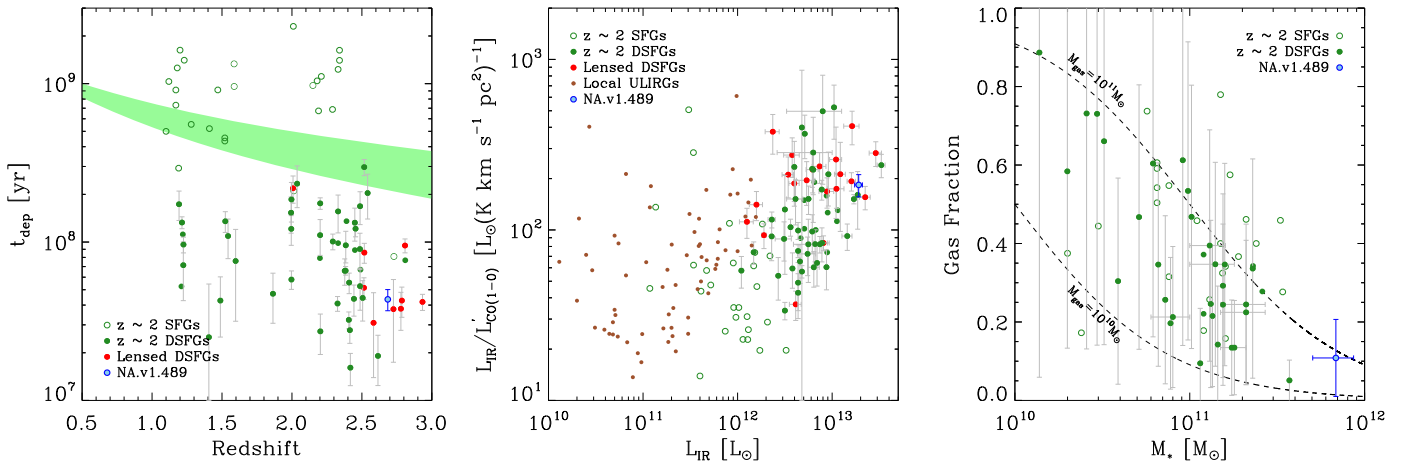


Figure 10. Left: evolution of the gas depletion timescale ($t_{\text{dep}} \equiv M_{\text{gas}}[M_{\odot}]/\text{SFR}[M_{\odot} \text{ yr}^{-1}]$) out to $z \sim 3$. The open symbols show the gas depletion for normal and lensed star-forming galaxies (Genzel et al. 2010; Dessauges-Zavadsky et al. 2015) compared to the shorter timescales seen for SMGs (filled green symbols; Frayer et al. 2008; Ivison et al. 2010b, 2011, 2013; Bothwell et al. 2013). The shaded area shows the predicted evolution of main-sequence galaxies at $z < 3$ (Davé et al. 2012; Saintonge et al. 2013). NA.v1.489 has a gas depletion timescale of 43 Myr, which is much lower than the SFGs at similar redshifts and consistent with lensed SMGs identified with the South Pole Telescope (SPT; Aravena et al. 2016) and from Thomson et al. (2012) at similar redshifts. Middle: star formation efficiency (SFE) vs. infrared luminosity (L_{IR} ; rest-frame 8–1000 μm) of NA.v1.489 compared to local ULIRGs (Papadopoulos et al. 2012) and high-redshift star-forming galaxies and SMGs. Right: molecular gas fraction ($f_{\text{g}} \equiv M_{\text{g}}/M_* + M_{\text{g}}$) as a function of stellar mass. NA.v1.489 has a low gas fraction compared to SMGs at similar redshifts, which could be indicating that the galaxy is toward the end of the star formation phase with near complete mass build-up. The dashed lines show the tracks for constant gas masses of $10^{10} M_{\odot}$ and $10^{11} M_{\odot}$.

normal star-forming galaxies and SMGs at similar and lower redshifts. The star formation rate efficiency of NA.v1.489 ($\text{SFE} \equiv L_{\text{IR}}/L'_{\text{CO}}$) is much higher than that of normal star-forming galaxies. The intense star formation in NA.v1.489 is not only because of the huge molecular gas reservoirs, which is comparable in some cases to those of massive star-forming galaxies (Genzel et al. 2010, 2015; Tacconi et al. 2013), but also to the higher SFE that is also observed in other high- z SMGs (Fu et al. 2013). Figure 10 shows the SFE of NA.v1.489 as a function of infrared luminosity (L_{IR} ; rest-frame 8–1000 μm) compared to the normal star-forming galaxies and SMGs. NA.v1.489 in particular has a higher SFE compared to normal star-forming galaxies and local ULIRGs, which is also observed in other SMGs at similar redshift (Fu et al. 2012). NA.v1.489, in particular, has a low gas fraction (with $f_{\text{g}} = 11\%$) compared to less massive normal star-forming galaxies and SMGs (Figure 10). Given the high stellar mass and low gas fraction, NA.v1.489 is an SMG that likely has already formed most of the stars.

The molecular gas mass as measured by the CO line luminosity depends on the assumed value for the conversion factor (α_{CO}). One of the main uncertainties in determining the total gas mass in fact lies with the uncertainties associated with the CO – H₂ conversion factor α_{CO} (Narayanan et al. 2012; Spilker et al. 2015). In this work, we assumed a conversion factor of $\alpha_{\text{CO}} = 0.8 M_{\odot}(\text{K km s}^{-1} \text{pc}^2)^{-1}$ to estimate the total molecular gas mass from CO observations. This is lower than the assumed value for the Milky Way ($\alpha_{\text{CO,MW}} = 4.36 M_{\odot}(\text{K km s}^{-1} \text{pc}^2)^{-1}$ measured from direct observations of molecular hydrogen and CO; Strong & Mattox 1996; Leroy et al. 2011; Bolatto et al. 2013) and that of nearby and high-redshift normal star-forming galaxies (Sandstrom et al. 2013; Tacconi et al. 2013). The lower conversion factor is more favored for extreme starburst due to the higher gas temperature and velocity dispersions (Narayanan et al. 2011, 2012; Papadopoulos et al. 2012; Bolatto et al. 2013), with the higher values overestimating the molecular gas mass in these systems

(Downes et al. 1993; Solomon et al. 1997). This is supported by the dust temperature measured for NA.v1.489, which could be a proxy for gas temperature (Yao et al. 2003). For normal star-forming galaxy analogs of NA.v1.489 (i.e., at similar stellar mass and redshift), α_{CO} could be measured given the metallicity-dependent relation provided by Genzel et al. (2015) (see Equations (6)–(8) in that paper; see also Dessauges-Zavadsky et al. 2016), where metallicity is estimated at the redshift and stellar mass of NA.v1.489 following the mass–metallicity relation (Erb et al. 2006; Maiolino et al. 2008; Wuyts et al. 2014; Zahid et al. 2014; see Equation (12) in Genzel et al. 2015). This yields a higher α_{CO} compared to what is assumed for starbursts, overestimating the molecular gas. Given the uncertainties, one could derive a possible range of molecular gas masses following Ivison et al. (2011) for a range of possible conversion factors. Here we report the gas mass estimate based on $\alpha_{\text{CO}} = 0.8 M_{\odot}(\text{K km s}^{-1} \text{pc}^2)^{-1}$, which is consistent with what was discussed above.

We investigate the far-infrared and radio properties of NA.v1.489 by looking at the FIR/radio ratio ($q_{\text{IR}} \equiv \log_{10}(S_{\text{IR}}/3.75 \times 10^{12} \text{ W m}^{-2}) - \log_{10}(S_{1.4 \text{ GHz}}/\text{W m}^{-2} \text{ Hz}^{-1})$) and how it compares with that of SMGs at similar and lower redshifts. We measured a $q_{\text{IR}} = 3.22$ for NA.v1.489, which is consistent with the average value derived for samples of far-infrared-selected galaxies at lower redshifts (Ivison et al. 2010a), the existence of which reflects the correlation between the processes that produce the underlying emissions, namely, star formation activity and synchrotron radiation from supernova processes contributing to FIR and radio emission, respectively (Yun et al. 2001; Bell 2003; Chapman et al. 2005; Ivison et al. 2010a; Elbaz et al. 2011; Pannella et al. 2015). The measured q_{IR} is consistent with low-redshift (Ivison et al. 2010a; Michałowski et al. 2010a) and high-redshift estimates (Pannella et al. 2015) as well as the average value for SMGs (Ivison et al. 2010a; Pannella et al. 2015). In fact, Ivison et al. (2010a) showed that the ratio is not evolving with time. The measured radio luminosity of NA.v1.489 ($L_{1.4} = 4.3 \times 10^{24} \text{ W Hz}^{-1}$) and the FIR/radio ratio indicate that NA.

v1.489 is not dominated by a radio-loud AGN (with $L_{1.4} \geq 10^{25} \text{ W Hz}^{-1}$) or having a radio excess (with $q_{\text{IR}} \leq 1.64$), as defined by Yun et al. (2001). The radio luminosity ($L_{1.4 \text{ GHz}}$) as measured by the JVLA yields an SFR $\sim 2560 \pm 414 M_{\odot} \text{ yr}^{-1}$ using the calibration in Pannella et al. (2015). This agrees with the SFR measured previously from the infrared luminosity derived from the multiband SED fit with the difference associated with the uncertainties that exist in the calibrations.

6. Summary and Conclusion

We have presented a detailed study of a massive *Herschel*/SPIRE-detected SMG at $z = 2.685$, gravitationally lensed by a *Spitzer*- and *WISE*-detected cluster at $z \sim 1$. We provide detailed lens modeling of the system through combined Keck and Gemini spectroscopic and imaging observations used to identify foreground cluster members and lensing multiple images. Our best lens model provides a lensing magnification of $\mu_{\text{star}} = 2.10$ and $\mu_{\text{dust}} = 2.02$ for the stellar and dust emissions, respectively, for NA.v1.489. Multiband SED fitting, corrected for the lensing magnification, provides the physical properties of NA.v1.489, including stellar mass (M_{\star}), total infrared luminosity (L_{IR} ; rest-frame 8–1000 μm), dust mass (M_{d}), and dust temperature (T_{d}); see Table 2. We further derived the total molecular gas and explored the ionization state of the gas from spectroscopic observations of the CO molecular emission lines. The combined physical properties derived from the SED fits and spectroscopic molecular CO line observations reveal that NA.v1.489 is a very massive SMG with SFR $\sim 2000 M_{\odot} \text{ yr}^{-1}$, putting it as one of the most extreme starbursts during the peak epoch of star formation, without a dominant AGN mode. The low- J molecular line luminosities revealed the existence of a large reservoir of molecular gas that is being rapidly converted into stars at a much higher pace compared to that of local ULIRGs (see Figure 10). This, combined with the measured low gas fraction ($f_{\text{g}} = 11\%$) and high stellar mass, shows that NA.v1.489 has already assembled most of its mass and is most likely on its way to becoming quiescent, forming a progenitor for the most massive early-type galaxies found in the local universe.

Observations of this galaxy seem to suggest that the location of SMGs on an SFR– M_{\star} diagram is consistent with the main sequence of star formation at the very massive end (Figure 9; Speagle et al. 2014) while still being above the relation which is supported by excessive star formation rate driving the intense infrared luminosities. This is in contrast to less massive SMGs with much higher observed SFRs compared to normal star-forming galaxies at similar stellar masses at $z \sim 2$ (Figure 9; Tacconi et al. 2010; Magnelli et al. 2012). As discussed above, this indicates that the very massive SMGs are on their way to becoming quiescent systems. We note here that in addition to the uncertainties associated with stellar mass (which we addressed in Section 4), uncertainties in the magnifications measured from the lens model could also lead to a high stellar mass. To test the robustness of the derived magnifications in the lens model, we recomputed the magnification using the MCMC maximum likelihood, which yielded the original magnification factor.

One of the main contributing factors to the transition of galaxies from a star-forming phase to that of quiescence is the feedback associated with AGN activity (Sijacki et al. 2007; Feruglio et al. 2010; Cicone et al. 2014) diluting and heating up

the molecular gas, ceasing star formation (Scannapieco et al. 2005). This generally begins with the central black hole gaining mass through constant accretion after which the AGN is ignited (Hopkins et al. 2016). The AGN signature has been observed in SEDs of SMGs in the mid-infrared and X-ray (Alexander et al. 2005; Valiante et al. 2007; Laird et al. 2010). The far-infrared luminosities are however believed to be mainly driven by star formation activity rather than an AGN (Magnelli et al. 2012). High emission line excitation ratios could be evidence for the presence of an AGN, although a lack of such highly excited lines does not necessarily rule out its existence. Combined X-ray through radio observations of distant SMGs along with mid-infrared constrained SEDs and emission line ratios are needed to study the presence and role of AGNs in detail. As discussed above, although we did not see a signature of a dominant AGN mode from CO line ratios in NA.v1.489, the presence of such a component could not be ruled out with current observations.

We wish to thank the anonymous referee for reading the original manuscript and providing useful suggestions. Financial support for this work was provided by NSF through AST-1313319 for H.N. and A.C. The UCI group also acknowledges support from *HST*-GO-14083.002-A, *HST*-GO-13718.002-A, and NASA NNX16AF38G grants. M.N. has received funding from the European Unions Horizon 2020 research and innovation program under the Marie Skłodowska-Curie grant agreement No 707601. D.R. acknowledges support from the National Science Foundation under grant number AST-1614213 to Cornell University. G.D.Z. acknowledges financial support from ASI/INAF agreement n. 2014-024-R.0. H.D. acknowledges financial support from the Spanish Ministry of Economy and Competitiveness (MINECO) under the 2014 Ramón y Cajal program MINECO RYC-2014-15686. I.O. and R.J.I. acknowledge support from the European Research Council in the form of the Advanced Investigator Programme, 321302, COSMICISM. J.L.W. is supported by a European Union COFUND/Durham Junior Research Fellowship under EU grant agreement number 267209, and acknowledges additional support from STFC (ST/L00075X/1). Some of the data presented herein were obtained at the W.M. Keck Observatory, which is operated as a scientific partnership among the California Institute of Technology, the University of California, and the National Aeronautics and Space Administration. The Observatory was made possible by the generous financial support of the W.M. Keck Foundation. The authors wish to recognize and acknowledge the very significant cultural role and reverence that the summit of Maunakea has always had within the indigenous Hawaiian community. We are most fortunate to have the opportunity to conduct observations from this mountain. Data presented herein were obtained using the UCI Remote Observing Facility, made possible by a generous gift from John and Ruth Ann Evans. Support for CARMA construction was derived from the Gordon and Betty Moore Foundation, the Kenneth T. and Eileen L. Norris Foundation, the James S. McDonnell Foundation, the Associates of the California Institute of Technology, the University of Chicago, the states of California, Illinois, and Maryland, and the National Science Foundation. Ongoing CARMA development and operations are supported by NSF grant ATI-0838178 to CARMA, and by the CARMA partner universities. The Submillimeter Array is a joint project between the Smithsonian

Astrophysical Observatory and the Academia Sinica Institute of Astronomy and Astrophysics and is funded by the Smithsonian Institution and the Academia Sinica.

References

- Alexander, D. M., Bauer, F. E., Chapman, S. C., et al. 2005, *ApJ*, 632, 736
- Aravena, M., Hodge, J. A., Wagg, J., et al. 2014, *MNRAS*, 442, 558
- Aravena, M., Spilker, J. S., Bethermin, M., et al. 2016, *MNRAS*, 457, 4406
- Barro, G., Faber, S. M., Pérez-González, P. G., et al. 2013, *ApJ*, 765, 104
- Becker, R. H., White, R. L., & Helfand, D. J. 1994, in *ASP Conf. Ser.* 61, *Astronomical Data Analysis Software and Systems III*, ed. D. R. Crabtree, R. J. Hanisch, & J. Barnes (San Francisco, CA: ASP), 165
- Bell, E. F. 2003, *ApJ*, 586, 794
- Bertin, E., & Arnouts, S. 1996, *A&AS*, 117, 393
- Béthermin, M., Daddi, E., Magdis, G., et al. 2015, *A&A*, 573, A113
- Blain, A. W. 1996, *MNRAS*, 283, 1340
- Blain, A. W., Smail, I., Ivison, R. J., & Kneib, J.-P. 1999, *MNRAS*, 302, 632
- Bolatto, A. D., Wolfire, M., & Leroy, A. K. 2013, *ARA&A*, 51, 207
- Bothwell, M. S., Smail, I., Chapman, S. C., et al. 2013, *MNRAS*, 429, 3047
- Bower, R. G., Benson, A. J., Malbon, R., et al. 2006, *MNRAS*, 370, 645
- Brinchmann, J., Charlot, S., White, S. D. M., et al. 2004, *MNRAS*, 351, 1151
- Bruzual, G., & Charlot, S. 2003, *MNRAS*, 344, 1000
- Bussmann, R. S., Gurwell, M. A., Fu, H., et al. 2012, *ApJ*, 756, 134
- Bussmann, R. S., Pérez-Fournon, I., Amber, S., et al. 2013, *ApJ*, 779, 25
- Bussmann, R. S., Riechers, D., Fialkov, A., et al. 2015, *ApJ*, 812, 43
- Cañameras, R., Nesvadba, N. P. H., Guery, D., et al. 2015, *A&A*, 581, A105
- Capak, P., Carilli, C. L., Lee, N., et al. 2008, *ApJL*, 681, L53
- Carilli, C. L., & Walter, F. 2013, *ARA&A*, 51, 105
- Casey, C. M., Berta, S., Béthermin, M., et al. 2012, *ApJ*, 761, 140
- Casey, C. M., Chapman, S. C., Beswick, R. J., et al. 2009, *MNRAS*, 399, 121
- Casey, C. M., Narayanan, D., & Cooray, A. 2014, *PhR*, 541, 45
- Chabrier, G. 2003, *PASP*, 115, 763
- Chapman, S. C., Blain, A. W., Smail, I., & Ivison, R. J. 2005, *ApJ*, 622, 772
- Charlot, S., & Fall, S. M. 2000, *ApJ*, 539, 718
- Cicone, C., Maiolino, R., Sturm, E., et al. 2014, *A&A*, 562, A21
- Cole, S., Aragon-Salamanca, A., Frenk, C. S., Navarro, J. F., & Zepf, S. E. 1994, *MNRAS*, 271, 781
- Condon, J. J., Cotton, W. D., Greisen, E. W., et al. 1998, *AJ*, 115, 1693
- Conroy, C. 2013, *ARA&A*, 51, 393
- da Cunha, E., Charlot, S., & Elbaz, D. 2008, *MNRAS*, 388, 1595
- da Cunha, E., Walter, F., Smail, I. R., et al. 2015, *ApJ*, 806, 110
- Daddi, E., Dannerbauer, H., Liu, D., et al. 2015, *A&A*, 577, A46
- Davé, R., Finlator, K., Oppenheimer, B. D., et al. 2010, *MNRAS*, 404, 1355
- Davé, R., Finlator, K., & Oppenheimer, B. D. 2012, *MNRAS*, 421, 98
- Decarli, R., Walter, F., Aravena, M., et al. 2016a, *ApJ*, 833, 69
- Decarli, R., Walter, F., Aravena, M., et al. 2016b, *ApJ*, 833, 70
- Dekel, A., Birnboim, Y., Engel, G., et al. 2009, *Natur*, 457, 451
- Dessauges-Zavadsky, M., Zamojski, M., Rujopakarn, W., et al. 2016, arXiv:1610.08065
- Dessauges-Zavadsky, M., Zamojski, M., Schaerer, D., et al. 2015, *A&A*, 577, A50
- Downes, D., & Solomon, P. M. 1998, *ApJ*, 507, 615
- Downes, D., Solomon, P. M., & Radford, S. J. E. 1993, *ApJL*, 414, L13
- Draine, B. T., & Lee, H. M. 1984, *ApJ*, 285, 89
- Dye, S., Furlanetto, C., Swinbank, A. M., et al. 2015, *MNRAS*, 452, 2258
- Eales, S., Dunne, L., Clements, D., et al. 2010, *PASP*, 122, 499
- Elbaz, D., Dickinson, M., Hwang, H. S., et al. 2011, *A&A*, 533, A119
- Engel, H., Tacconi, L. J., Davies, R. I., et al. 2010, *ApJ*, 724, 233
- Erb, D. K., Shapley, A. E., Pettini, M., et al. 2006, *ApJ*, 644, 813
- Faber, S. M., Phillips, A. C., Kibrick, R. I., et al. 2003, *Proc. SPIE*, 4841, 1657
- Fanaroff, B. L., & Riley, J. M. 1974, *MNRAS*, 167, 31P
- Feruglio, C., Maiolino, R., Piconcelli, E., et al. 2010, *A&A*, 518, L155
- Freyer, D. T., Harris, A. I., Baker, A. J., et al. 2011, *ApJL*, 726, L22
- Freyer, D. T., Ivison, R. J., Scoville, N. Z., et al. 1998, *ApJL*, 506, L7
- Freyer, D. T., Ivison, R. J., Scoville, N. Z., et al. 1999, *ApJL*, 514, L13
- Freyer, D. T., Koda, J., Pope, A., et al. 2008, *ApJL*, 680, L21
- Fu, H., Cooray, A., Feruglio, C., et al. 2013, *Natur*, 498, 338
- Fu, H., Jullo, E., Cooray, A., et al. 2012, *ApJ*, 753, 134
- Furlong, M., Bower, R. G., Theuns, T., et al. 2015, *MNRAS*, 450, 4486
- Gavazzi, R., Cooray, A., Conley, A., et al. 2011, *ApJ*, 738, 125
- Genzel, R., Burkert, A., Bouché, N., et al. 2008, *ApJ*, 687, 59
- Genzel, R., Tacconi, L. J., Gracia-Carpio, J., et al. 2010, *MNRAS*, 407, 2091
- Genzel, R., Tacconi, L. J., Lutz, D., et al. 2015, *ApJ*, 800, 20
- Granato, G. L., De Zotti, G., Silva, L., Bressan, A., & Danese, L. 2004, *ApJ*, 600, 580
- Greve, T. R., Bertoldi, F., Smail, I., et al. 2005, *MNRAS*, 359, 1165
- Griffin, M. J., Abergel, A., Abreu, A., et al. 2010, *A&A*, 518, L3
- Hainline, L. J., Blain, A. W., Smail, I., et al. 2011, *ApJ*, 740, 96
- Harris, A. I., Baker, A. J., Frayer, D. T., et al. 2012, *ApJ*, 752, 152
- Hayward, C. C., Kereš, D., Jonsson, P., et al. 2011, *ApJ*, 743, 159
- Hayward, C. C., & Smith, D. J. B. 2015, *MNRAS*, 446, 1512
- Hemmati, S., Miller, S. H., Mobasher, B., et al. 2014, *ApJ*, 797, 108
- Hemmati, S., Mobasher, B., Darvish, B., et al. 2015, *ApJ*, 814, 46
- Hemmati, S., Yan, L., Diaz-Santos, T., et al. 2017, *ApJ*, 834, 36
- Ho, P. T. P., Moran, J. M., & Lo, K. Y. 2004, *ApJL*, 616, L1
- Hodge, J. A., Riechers, D., Decarli, R., et al. 2015, *ApJL*, 798, L18
- Hopkins, P. F., Cox, T. J., Hernquist, L., et al. 2013, *MNRAS*, 430, 1901
- Hopkins, P. F., Hernquist, L., Cox, T. J., & Kereš, D. 2008, *ApJS*, 175, 356
- Hopkins, P. F., Torrey, P., Faucher-Giguère, C.-A., Quataert, E., & Murray, N. 2016, *MNRAS*, 458, 816
- Home, K. 1986, *PASP*, 98, 609
- Hwang, H. S., Elbaz, D., Magdis, G., et al. 2010, *MNRAS*, 409, 75
- Iglesias-Páramo, J., Buat, V., Hernández-Fernández, J., et al. 2007, *ApJ*, 670, 279
- Ivison, R. J., Magnelli, B., Ibar, E., et al. 2010a, *A&A*, 518, L31
- Ivison, R. J., Papadopoulos, P. P., Smail, I., et al. 2011, *MNRAS*, 412, 1913
- Ivison, R. J., Smail, I., Barger, A. J., et al. 2000, *MNRAS*, 315, 209
- Ivison, R. J., Smail, I., Le Borgne, J.-F., et al. 1998, *MNRAS*, 298, 583
- Ivison, R. J., Swinbank, A. M., Smail, I., et al. 2013, *ApJ*, 772, 137
- Ivison, R. J., Swinbank, A. M., Swinyard, B., et al. 2010b, *A&A*, 518, L35
- Jullo, E., & Kneib, J.-P. 2009, *MNRAS*, 395, 1319
- Jullo, E., Kneib, J.-P., Limousin, M., et al. 2007, *NJPh*, 9, 447
- Kauffmann, G., Heckman, T. M., White, S. D. M., et al. 2003, *MNRAS*, 341, 33
- Kauffmann, G., White, S. D. M., & Guiderdoni, B. 1993, *MNRAS*, 264, 201
- Kennicutt, R. C., Jr. 1998, *ARA&A*, 36, 189
- Kneib, J.-P., Ellis, R. S., Smail, I., Couch, W. J., & Sharples, R. M. 1996, *ApJ*, 471, 643
- Koprowski, M. P., Dunlop, J. S., Michałowski, M. J., et al. 2016, *MNRAS*, 458, 4321
- Koprowski, M. P., Dunlop, J. S., Michałowski, M. J., Cirasuolo, M., & Bowler, R. A. A. 2014, *MNRAS*, 444, 117
- Kormendy, J., & Kennicutt, R. C., Jr. 2004, *ARA&A*, 42, 603
- Krujissen, J. M. D., Longmore, S. N., Elmegreen, B. G., et al. 2014, *MNRAS*, 440, 3370
- Laird, E. S., Nandra, K., Pope, A., & Scott, D. 2010, *MNRAS*, 401, 2763
- Law, D. R., Steidel, C. C., Erb, D. K., et al. 2009, *ApJ*, 697, 2057
- Lawrence, A., Warren, S. J., Almaini, O., et al. 2007, *MNRAS*, 379, 1599
- Leroy, A. K., Bolatto, A., Gordon, K., et al. 2011, *ApJ*, 737, 12
- Leroy, A. K., Walter, F., Sandstrom, K., et al. 2013, *AJ*, 146, 19
- Madau, P., & Dickinson, M. 2014, *ARA&A*, 52, 415
- Magdis, G. E., Daddi, E., Béthermin, M., et al. 2012, *ApJ*, 760, 6
- Magdis, G. E., Elbaz, D., Hwang, H. S., et al. 2010, *MNRAS*, 409, 22
- Magnelli, B., Lutz, D., Saintonge, A., et al. 2014, *A&A*, 561, A86
- Magnelli, B., Lutz, D., Santini, P., et al. 2012, *A&A*, 539, A155
- Maiolino, R., Nagao, T., Grazian, A., et al. 2008, *A&A*, 488, 463
- Mancuso, C., Lapi, A., Shi, J., et al. 2016, *ApJ*, 823, 128
- Mannucci, F., Cresci, G., Maiolino, R., Marconi, A., & Gnerucci, A. 2010, *MNRAS*, 408, 2115
- Messias, H., Dye, S., Nagar, N., et al. 2014, *A&A*, 568, A92
- Michałowski, M., Hjorth, J., & Watson, D. 2010a, *A&A*, 514, A67
- Michałowski, M. J., Dunlop, J. S., Cirasuolo, M., et al. 2012, *A&A*, 541, A85
- Michałowski, M. J., Dunlop, J. S., Koprowski, M. P., et al. 2017, *MNRAS*, 469, 492
- Michałowski, M. J., Hayward, C. C., Dunlop, J. S., et al. 2014, *A&A*, 571, A75
- Michałowski, M. J., Hjorth, J., Castro Cerón, J. M., & Watson, D. 2008, *ApJ*, 672, 817
- Michałowski, M. J., Hjorth, J., Malesani, D., et al. 2009, *ApJ*, 693, 347
- Michałowski, M. J., Hjorth, J., & Watson, D. 2010b, *A&A*, 514, A67
- Michałowski, M. J., Watson, D., & Hjorth, J. 2010c, *ApJ*, 712, 942
- Mocanu, L. M., Crawford, T. M., Vieira, J. D., et al. 2013, *ApJ*, 779, 61
- Narayanan, D., Krumholz, M., Ostriker, E. C., & Hernquist, L. 2011, *MNRAS*, 418, 664
- Narayanan, D., Krumholz, M. R., Ostriker, E. C., & Hernquist, L. 2012, *MNRAS*, 421, 3127
- Narayanan, D., Turk, M., Feldmann, R., et al. 2015, *Natur*, 525, 496
- Navarro, J. F., Frenk, C. S., & White, S. D. M. 1996, *ApJ*, 462, 563
- Nayeri, H., Keele, M., Cooray, A., et al. 2016, *ApJ*, 823, 17

- Nayyeri, H., Mobasher, B., Hemmati, S., et al. 2014, *ApJ*, 794, 68
- Negrello, M., Amber, S., Amvrosiadis, A., et al. 2017, *MNRAS*, 465, 3558
- Negrello, M., Hopwood, R., De Zotti, G., et al. 2010, *Sci*, 330, 800
- Negrello, M., Hopwood, R., Dye, S., et al. 2014, *MNRAS*, 440, 1999
- Noeske, K. G., Weiner, B. J., Faber, S. M., et al. 2007, *ApJL*, 660, L43
- Oke, J. B., & Gunn, J. E. 1983, *ApJ*, 266, 713
- Oteo, I., Ivison, R. J., Dunne, L., et al. 2016, *ApJ*, 827, 34
- Ott, S. 2010, in ASP Conf. Ser. 434, *Astronomical Data Analysis Software and Systems XIX*, ed. Y. Mizumoto, K.-I. Morita, & M. Ohishi (San Francisco, CA: ASP), 139
- Pannella, M., Elbaz, D., Daddi, E., et al. 2015, *ApJ*, 807, 141
- Papadopoulos, P. P., van der Werf, P. P., Xilouris, E. M., et al. 2012, *MNRAS*, 426, 2601
- Peng, C. Y., Ho, L. C., Impey, C. D., & Rix, H.-W. 2002, *AJ*, 124, 266
- Pilbratt, G. L., Riedinger, J. R., Passvogel, T., et al. 2010, *A&A*, 518, L1
- Rawle, T. D., Egami, E., Bussmann, R. S., et al. 2014, *ApJ*, 783, 59
- Riechers, D. A., Bradford, C. M., Clements, D. L., et al. 2013, *Natur*, 496, 329
- Riechers, D. A., Capak, P. L., Carilli, C. L., et al. 2010, *ApJL*, 720, L131
- Riechers, D. A., Carilli, C. L., Capak, P. L., et al. 2014, *ApJ*, 796, 84
- Riechers, D. A., Cooray, A., Omont, A., et al. 2011a, *ApJL*, 733, L12
- Riechers, D. A., Hodge, J., Walter, F., Carilli, C. L., & Bertoldi, F. 2011b, *ApJL*, 739, L31
- Rybak, M., Vegetti, S., McKean, J. P., Andreani, P., & White, S. D. M. 2015, *MNRAS*, 453, L26
- Saintonge, A., Lutz, D., Genzel, R., et al. 2013, *ApJ*, 778, 2
- Sandstrom, K. M., Leroy, A. K., Walter, F., et al. 2013, *ApJ*, 777, 5
- Scannapieco, E., Silk, J., & Bouwens, R. 2005, *ApJL*, 635, L13
- Scoville, N., Aussel, H., Sheth, K., et al. 2014, *ApJ*, 783, 84
- Scoville, N., Sheth, K., Aussel, H., et al. 2016, *ApJ*, 820, 83
- Sharon, C. E., Riechers, D. A., Hodge, J., et al. 2016, *ApJ*, 827, 18
- Shivaei, I., Reddy, N. A., Shapley, A. E., et al. 2015, *ApJ*, 815, 98
- Sijacki, D., Springel, V., Di Matteo, T., & Hernquist, L. 2007, *MNRAS*, 380, 877
- Silva, L., Granato, G. L., Bressan, A., & Danese, L. 1998, *ApJ*, 509, 103
- Solomon, P. M., Downes, D., Radford, S. J. E., & Barrett, J. W. 1997, *ApJ*, 478, 144
- Solomon, P. M., & Vanden Bout, P. A. 2005, *ARA&A*, 43, 677
- Speagle, J. S., Steinhardt, C. L., Capak, P. L., & Silverman, J. D. 2014, *ApJS*, 214, 15
- Spilker, J. S., Aravena, M., Marrone, D. P., et al. 2015, *ApJ*, 811, 124
- Stanford, S. A., Gonzalez, A. H., Brodwin, M., et al. 2014, *ApJS*, 213, 25
- Strandet, M. L., Weiss, A., Vieira, J. D., et al. 2016, *ApJ*, 822, 80
- Strong, A. W., & Mattox, J. R. 1996, *A&A*, 308, L21
- Su, T., Marriage, T. A., Asboth, V., et al. 2017, *MNRAS*, 464, 968
- Swinbank, A. M., Dye, S., Nightingale, J. W., et al. 2015, *ApJL*, 806, L17
- Swinbank, A. M., Papadopoulos, P. P., Cox, P., et al. 2011, *ApJ*, 742, 11
- Swinbank, A. M., Smail, I., Chapman, S. C., et al. 2010, *MNRAS*, 405, 234
- Symeonidis, M., Vaccari, M., Berta, S., et al. 2013, *MNRAS*, 431, 2317
- Tacconi, L. J., Genzel, R., Neri, R., et al. 2010, *Natur*, 463, 781
- Tacconi, L. J., Genzel, R., Smail, I., et al. 2008, *ApJ*, 680, 246
- Tacconi, L. J., Neri, R., Chapman, S. C., et al. 2006, *ApJ*, 640, 228
- Tacconi, L. J., Neri, R., Genzel, R., et al. 2013, *ApJ*, 768, 74
- Thomson, A. P., Ivison, R. J., Smail, I., et al. 2012, *MNRAS*, 425, 2203
- Timmons, N., Cooray, A., Nayyeri, H., et al. 2015, *ApJ*, 805, 140
- Toft, S., Smolčić, V., Magnelli, B., et al. 2014, *ApJ*, 782, 68
- Valiante, E., Lutz, D., Sturm, E., et al. 2007, *ApJ*, 660, 1060
- Valiante, E., Smith, M. W. L., Eales, S., et al. 2016, *MNRAS*, 462, 3146
- Wang, S. X., Brandt, W. N., Luo, B., et al. 2013, *ApJ*, 778, 179
- Wardlow, J. L., Cooray, A., De Bernardis, F., et al. 2013, *ApJ*, 762, 59
- Wardlow, J. L., Smail, I., Coppin, K. E. K., et al. 2011, *MNRAS*, 415, 1479
- Weiß, A., De Breuck, C., Marrone, D. P., et al. 2013, *ApJ*, 767, 88
- Wright, E. L., Eisenhardt, P. R. M., Mainzer, A. K., et al. 2010, *AJ*, 140, 1868
- Wuyts, E., Kurk, J., Förster Schreiber, N. M., et al. 2014, *ApJL*, 789, L40
- Wuyts, S., Förster Schreiber, N. M., van der Wel, A., et al. 2011, *ApJ*, 742, 96
- Yao, L., Seaquist, E. R., Kuno, N., & Dunne, L. 2003, *ApJ*, 588, 771
- Yun, M. S., Reddy, N. A., & Condon, J. J. 2001, *ApJ*, 554, 803
- Zahid, H. J., Dima, G. I., Kudritzki, R.-P., et al. 2014, *ApJ*, 791, 130